nature chemical biology

Article

https://doi.org/10.1038/s41589-025-01921-4

Unraveling Alzheimer's complexity with a distinct $A\beta_{42}$ fibril type and specific AV-45 binding

Received: 17 August 2023

Accepted: 14 April 2025

Published online: 10 June 2025

Check for updates

Qinyue Zhao[1,2,11], Youqi Tao[1,2,11], Yuxuan Yao[1,2], Kaien Liu[3,4], Shiran Lv[3,4], Bingyao Cui[1,2], Weidi Xiao[5], Tianyi Cao[1,2], Weidong Li[6], Feng Gao[7,8], Yong Shen[7,8], Chu Wang[5], Chao Ma[9], Wenying Qiu[9] ✉, Cong Liu[3,4,10] ✉ & Dan Li[1,2] ✉

Abnormal aggregation of amyloid-β protein (1–42) ($A\beta_{42}$) is the primary pathology in Alzheimer's disease (AD). Two types of $A\beta_{42}$ fibrils have been identified in the insoluble fraction of diseased human brains. Here, we report that the fraction previously deemed 'soluble' during sarkosyl extraction of AD brains actually harbors numerous amyloid fibrils, with a looser bundling than those in the insoluble fraction. Using cryo-electron microscopy (cryo-EM), we discover a third type (type III) of $A\beta_{42}$ fibril that is occasionally found in the soluble but not insoluble fraction of one AD brain. We also reveal that cryo-EM structures of $A\beta_{42}$ fibrils complexed with the positron emission tomography tracer AV-45 show a ligand-binding channel within type I but not type III $A\beta_{42}$ fibrils. In this binding channel, AV-45 engages with a vertical geometry. Through the discovery of this new structural polymorph of ex vivo $A\beta_{42}$ fibril, our study highlights the notable structural heterogeneity of Aβ fibrils among persons with AD.

Alzheimer's disease (AD) is the most common, progressive age-related neurodegenerative disease, often clinically characterized by memory loss and cognitive deficits[1–4]. Neuropathologically, AD is characterized by dramatic atrophy of the gray matter and aggregation of amyloid-β (Aβ) (amyloid plaques) and Tau (neurofibrillary tangles, NFTs)[5–7]. Despite the common pathology, the clinical phenotypes of AD exhibit conspicuous variability among cases[8–12]. A recent in situ investigation of Aβ fibrils in AD brains suggested the heterogeneous nature of fibrillar species within amyloid plaques[13]. Two types of ex vivo $A\beta_{42}$ fibrils have been identified in AD: type I fibrils are predominantly observed in sporadic AD, whereas type II fibrils are associated with familial AD and other neurodegenerative disorders[14]. Recent studies showed that ex vivo Aβ fibrils from Aβ precursor protein (APP) genetic variants, including Arctic mutation and Down syndrome, present Aβ fibril conformations different from types I and II, even though cases eventually develop into AD[15,16]. These structural studies indicate the high heterogeneity of Aβ fibril in different contexts of AD. In addition, in vitro studies, using Aβ fibrils amplified from ex vivo seeds extracted from AD brains, demonstrated the high potential of Aβ aggregation into structural variants with distinct pathological traits[17–20]. Therefore, considering the complicacy of AD pathologies and symptoms, more Aβ fibril polymorphs might exist in AD brains and are yet to be identified.

Currently, the extraction of amyloid fibrils, such as $A\beta_{42}$ and Tau fibrils from persons with AD[14,21] and α-synuclein (α-syn) fibrils from persons with Parkinson's disease (PD), mainly adopts the sarkosyl extraction method, sometimes with slight modifications of the protocol[22]. With this protocol, fibrils are mainly obtained from the insoluble fraction, which is normally referred to as the pellet after 100,000*g* ultracentrifugation. The supernatant at this purification step is regarded as soluble without amyloid fibrils and, thus, discarded[15,23–25].

In this study, we extracted amyloid fibrils using the sarkosyl extraction method from the brains of three persons with sporadic AD. These cases exhibited similar pathological phenotypes but distinct clinical manifestations. Surprisingly, we observed numerous amyloid fibrils

A full list of affiliations appears at the end of the paper. ✉e-mail: qiuwy73@126.com; liulab@sioc.ac.cn; lidan2017@sjtu.edu.cn

https://doi.org/10.1038/s41589-025-01921-4

Table 1 | Pathological diagnoses and amyloid fibril components in the soluble fractions of the brains from three persons with AD

Basic information				Pathological diagnoses		Soluble fibril components[a]		
Identifier	Gender	Age (years)	Postmortem interval (h)	Clinical pathology	Neurological pathology	Type I $A\beta_{42}$	Type III $A\beta_{42}$	TMEM106B
AD1	Male	83	4.5	Progressive dementia, parkinsonism behaviors (muscular hypertonia), cerebral infarction	$A\beta_{42}^+$ (dense plaques and focal deposits), $A\beta_{40}^+$ (sparse plaque cores and severe cerebral amyloid deposit), pTau$^+$ (Tau NFTs and threads), α-syn$^+$ (scattered Lewy bodies and Lewy neurites) and TMEM106B$^+$ (ring-like cytoplasmic inclusions and filamentous inclusions).	35.6%	29.7%	34.7%
AD2	Female	84	6	Dementia, abdominal aortic aneurysm, cardiac failure	$A\beta_{42}^+$ (dense plaques), $A\beta_{40}^+$ (sparse plaque cores), pTau$^+$, α-syn$^+$ and TMEM106B$^+$ (deposits consistent with the above).	78.2%	\	21.8%
AD3	Male	89	4.5	Dementia, parkinsonism behaviors (Parkinson's respiratory failure)		49.2%	\	50.8%

[a]The soluble fraction (S2) of sarkosyl extraction, determined by cryo-EM.

in the previously considered soluble fraction in all cases, which were more dispersed than those in the insoluble fraction. More importantly, we identified a new type of $A\beta_{42}$ fibril (termed type III), which exclusively presented in the soluble fraction of one of the persons with AD. We further determined the structures of type I and type III $A\beta_{42}$ fibrils in complex with AV-45, a Food and Drug Administration (FDA)-approved Aβ tracer that is widely used clinically for AD diagnosis, using cryo-electron microscopy (cryo-EM)[26]. The structures revealed that AV-45 thrusts into an interior ligand-binding channel in the fibril core of the type I fibril, while the type III fibril lacks such a channel for AV-45 binding. Collectively, the finding of type III $A\beta_{42}$ fibrils suggests resurveillance of amyloid components in the soluble fraction of sarkosyl extraction and, more importantly, showcases the heterogeneity of fibril among persons with AD. In addition, different mechanisms for AV-45 binding to different $A\beta_{42}$ fibrils warrant caution during the readout of Aβ tracers.

Results

Neuropathological diagnosis of persons with AD

Three persons with sporadic AD were used in our study, termed AD1 (male, 83 years), AD2 (female, 84 years) and AD3 (male, 89 years) (Table 1). Among them, two cases, AD1 and AD3, manifested parkinsonian behaviors, such as muscular hypertonia (for AD1) and Parkinson's respiratory failure (for AD3). AD1, who died from cerebral infarction, also showed severe cerebral amyloid angiopathy (CAA).

Immunohistochemistry (IHC) staining was used to characterize the neuropathological features of the three participants. Numerous dense plaques formed by $A\beta_{42}$ were observed in frontal cortex of all three cases, while another appearance of $A\beta_{42}$ plaques (focal deposits with a spherical dense core surrounded by a loosely packed rim) was only observed in AD1 (Fig. 1a). Meanwhile, we observed sparse plaque cores of $A\beta_{40}$ in all three cases (Fig. 1b). In line with clinical manifestation of CAA, blood vessel deposits of $A\beta_{40}$ were observed in AD1 (Fig. 1b and Table 1). In all three cases, we also observed NFTs and threads using AT8 (a monoclonal antibody to paired helical filament Tau phosphorylated at S202/T205) (Fig. 1c). Scattered Lewy bodies and Lewy neurites were also stained in all cases by Syn303 (a monoclonal antibody recognizing residues 1–5 of human α-syn) (Fig. 1d). We also performed IHC staining with an antibody targeting residues 204–253 of transmembrane protein 106B (TMEM106B), which was recently identified to form age-related amyloid fibrils[27–30]. Consistent with previous report[27,31], we observed numerous TMEM106B puncta in all cases, which exhibited two morphologies: ring-like cytoplasmic inclusions surrounding the nuclei and filamentous inclusions (Fig. 1e). Collectively, these observations neuropathologically confirm the AD diagnosis of the three participants, while their neuropathological differences indicate the heterogeneity of AD pathology among the cases, in accordance with their variations in disease phenotypes.

Numerous amyloid fibrils exist in the soluble fraction of AD brains

We then used the well-established sarkosyl-based extraction method to isolate amyloid fibrils from the frontal cortex of the three AD cases (Fig. 2a and Extended Data Fig. 1)[14,30]. Following the protocol, after 100,000*g* ultracentrifugation, amyloid fibrils are precipitated in the insoluble fraction (P2) (Extended Data Fig. 1). However, as we examined the supernatant (S2) by negative-staining transmission EM (NS-TEM), we surprisingly observed a notable number of amyloid fibrils in all three cases (Extended Data Fig. 1). Consistent with this, a recent study also observed abundant Aβ fibrils in the soluble fraction of AD brains when adopting the aqueous extraction method[32]. To uncover the identity of the fibrils in the sarkosyl-soluble fraction (referred to as the soluble fraction hereafter), we continued to perform the same purification step as for the insoluble fraction (Extended Data Fig. 1). The obtained fibril samples were further used for cryo-EM analysis.

Identification of the soluble fibril components by cryo-EM

Micrographs were collected on a 300-kV Titan Krios microscope. Fibrils were manually picked from the micrographs for helical reconstruction. Reference-free two-dimensional (2D) class averaging and three-dimensional (3D) classifications identified that the soluble fractions of the three cases all contained type I $A\beta_{42}$ and TMEM106B fibrils (Table 1, Fig. 2b, Supplementary Fig. 2 and Supplementary Table 1). We obtained density maps at a resolution of 3.0–3.4 Å for the type I $A\beta_{42}$ fibrils (Fig. 2b, Extended Data Fig. 2 and Supplementary Table 2) and built structural models accordingly (Extended Data Fig. 3). The structures of type I $A\beta_{42}$ fibrils in the soluble fractions of different AD brains were nearly identical and also highly similar to those isolated from the insoluble fraction of AD brains[14] (Extended Data Fig. 3e). Because type I $A\beta_{42}$ fibrils are mainly found in persons with sporadic AD[14], this result further confirms the primary pathology of the three AD cases.

Strikingly, in addition to the type I $A\beta_{42}$ and TMEM106B fibrils, we found a new type of $A\beta_{42}$ fibril, termed type III, occupying a substantial proportion (29.7%) of the soluble fraction of AD1 brain (Table 1 and Fig. 2b), which was observed neither in AD2 or AD3 (Fig. 2b) nor in the insoluble fraction of AD1 (Supplementary Fig. 2). This result indicates that the soluble fraction contains unique fibrils that are not present in the insoluble fraction and occasionally exist in AD.

To understand the difference between the fibrils in the soluble and insoluble fractions, we retrieved the cryo-EM particles from the

https://doi.org/10.1038/s41589-025-01921-4

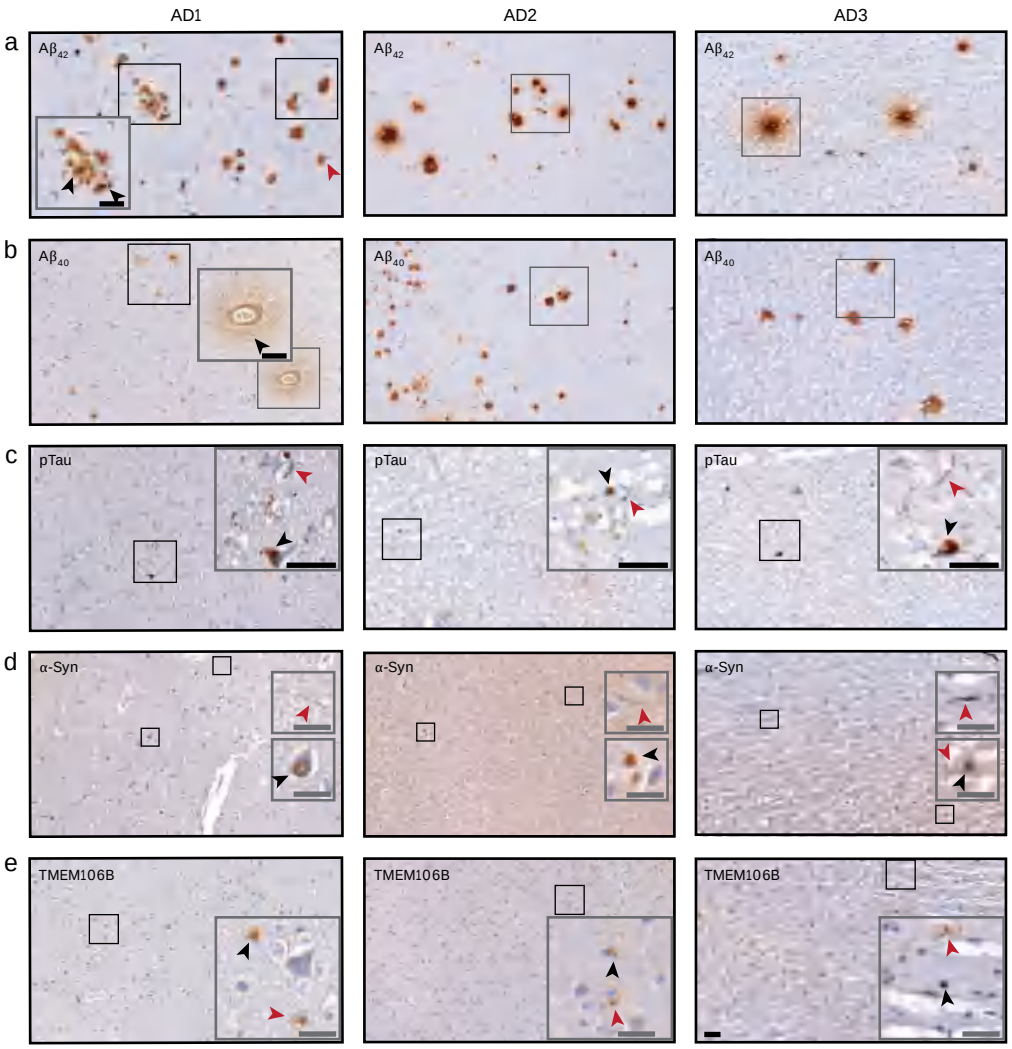

Fig. 1 | IHC of the brain slices derived from three persons with AD. Staining of amyloid deposits (brown) in the frontal cortex sections. The nuclei are counterstained in blue. Zoomed-in views are shown of representative deposits, indicated with arrowheads. Scale bars: black line, 100 μm; gray line, 25 μm. **a**, Aβ plaques stained with $Aβ_{42}$ antibody (1:250). In AD1, two plaque morphologies were observed: focal deposits and dense plaques; the former is indicated with black arrows. **b**, $Aβ_{40}$ deposits stained with $Aβ_{40}$ antibody (1:1,000). Plaque cores were observed in all three AD cases. Blood vessel deposits were identified only in AD1 (black arrow). **c**, Tau deposits stained with AT8 (1:1,000). Both Tau NFTs (black arrow) and Tau threads (red arrow) were observed in all cases. **d**, α-Syn inclusions stained with α-syn monoclonal antibody Syn303 (1:250). Scattered Lewy bodies (black arrow) and Lewy neurites (red arrow) were observed in all cases. **e**, TMEM106B puncta stained with TMEM106B monoclonal antibody (1:250). Ring-like cytoplasmic inclusions (black arrow) and filamentous inclusions (red arrow) are indicated.

original micrographs (Fig. 3a,b)[33]. The result remarkably showed that, after 100,000*g* ultracentrifugation, fibrils in the soluble fraction were generally well dispersed with few clustered fibrils; in contrast, fibrils in the insoluble fraction tended to bundle together with notably more crossover points per unit length of each fibril (Fig. 3c and Extended Data Fig. 4). Furthermore, we noticed that, although type I $Aβ_{42}$ fibrils existed in both soluble and insoluble fractions, they had different extra densities in the cryo-EM maps, indicating different surface modifications (Supplementary Fig. 3). These results indicate that, consistent with the ultracentrifugal behaviors of the fibrils, the soluble fibrils were less bundled than the insoluble fibrils and, thus, featured lower densities; this feature might be independent of fibril structures but defined by surface modifications.

To further probe the surface modifications of the soluble and insoluble fibrils, we conducted liquid chromatography–tandem mass spectrometry (LC–MS/MS) on the sarkosyl-soluble and insoluble fractions extracted from the AD1 brain. Several common post-translational modifications (PTMs) were found in both fractions, such as N-terminal pyroglutamate and oxidation of methionine (Supplementary Fig. 4a). Notably, we also identified some featured PTMs in the sarkosyl-insoluble fraction, including carbonyl modification on S26 (Supplementary Fig. 4b) and pyruvic acridinyl on K28 (Supplementary Fig. 4c). Furthermore, we performed label-free quantification of the proteomes in the two fractions (Supplementary Fig. 5a). We identified 34 proteins upregulated (Supplementary Fig. 5b and Supplementary Table 3) and 25 proteins downregulated (Supplementary Fig. 5b and Supplementary Table 4) in the sarkosyl-insoluble fraction. The Gene Ontology annotations support that the two different fractions contained different coaggregated proteins (Supplementary Fig. 5c,d). Together with different PTM patterns, these modifications may lead to different physicochemical properties, potentially resulting in varied degrees of pathological toxicity.

Cryo-EM structure of the type III $Aβ_{42}$ fibril

After analysis of the fibril components in the AD cases, a novel polymorph of $Aβ_{42}$ fibril termed type III was found in AD1. The type III $Aβ_{42}$

https://doi.org/10.1038/s41589-025-01921-4

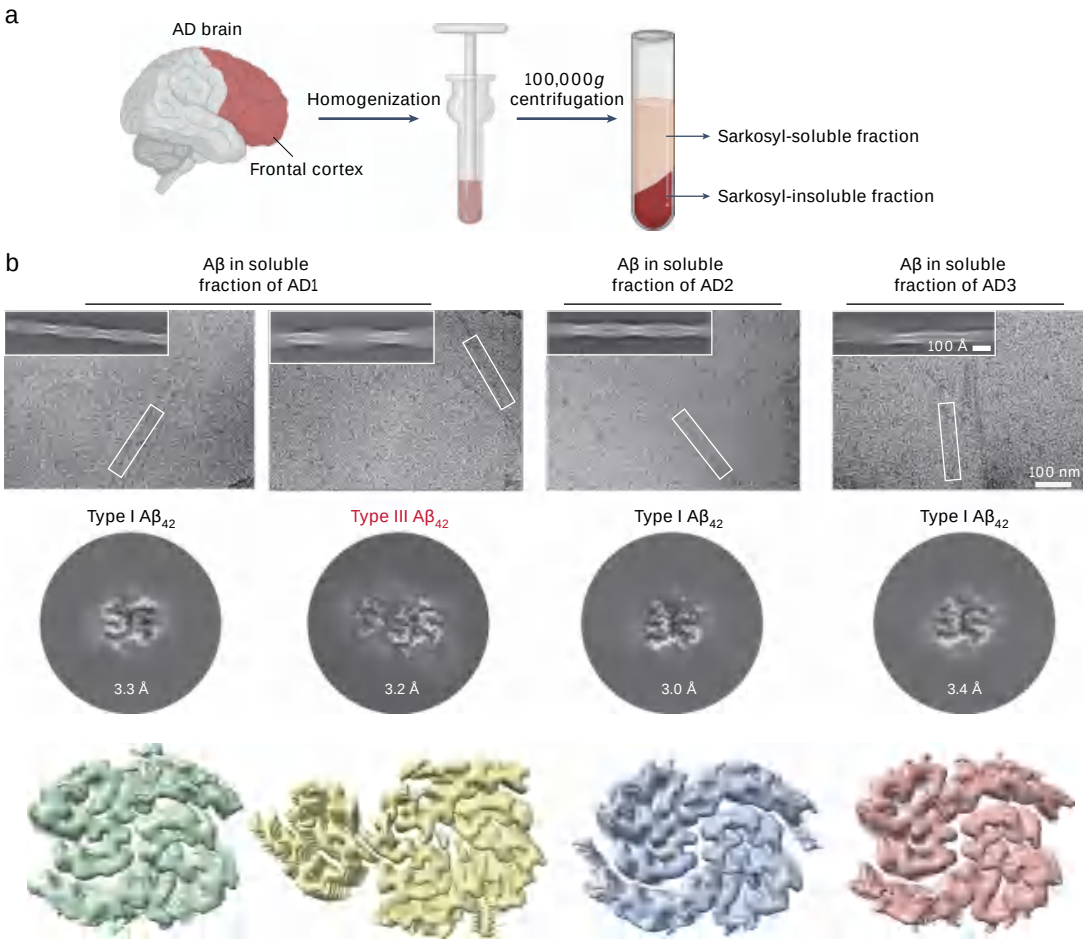

Fig. 2 | Characterization of $A\beta_{42}$ amyloid fibrils in the soluble fraction of AD brains. a, Schematic illustration of soluble and insoluble fractions of the sarkosyl-based extraction method. Created with BioRender.com. **b**, Top, cryo-EM micrographs of $A\beta_{42}$ fibrils in the soluble fraction extracted from brains of three persons with AD. The 2D class averages are shown as insets. Middle, central slices of 3D maps. Bottom, reconstructed density maps.

fibril features a left-handed helical twist (Extended Data Fig. 5), with a pitch of ~87.90 nm, twist angle of −1.97° and helical rise of 4.81 Å (Fig. 4a). Unlike types I and II that are composed of two identical protofilaments, the type III $A\beta_{42}$ fibril consists of three protofilaments. Among them, two identical S-shaped protofilaments tangle with extra densities of cofactors in between; a third related S-shaped protofilament is further entangled (Fig. 4a).

To understand the distinct formation of type III $A\beta_{42}$ fibril, we unambiguously built a structural model on the basis of 3.2-Å density map (Fig. 4b, Extended Data Fig. 2 and Supplementary Table 2). The type III $A\beta_{42}$ fibril contains two related S-shaped folds. One is shared by the identical chains A and B with an extended tail (Extended Data Fig. 6a,b). This fold (referred to as fold 1′) has high structural similarities with the Aβ fold in the type I fibril (referred to as fold 1) at two regions including residues 9–18 and 27–42 (Fig. 4c,d). While conformational variations at the linker region of residues 18–27 twist the overall geometry of the S fold and lead to two similar (root-mean-square deviation (r.m.s.d.) of 0.480 Å over ten Cα atoms) but notably different folds (Fig. 4d). The other fold of $A\beta_{42}$ in the type III fibril represented by chain C is more compact with a short tail (Fig. 4d and Extended Data Fig. 6a), which is nearly identical to the $A\beta_{42}$ fold in the type II fibril (referred to as fold 2) (Extended Data Fig. 6c). In addition, although the N-terminal fragment 1–8/11 is invisible in the cryo-EM structure, the sarkosyl-soluble fibrils of AD1 contain full-length $A\beta_{42}$ characterized by MS/MS, western blot and immunogold NS-TEM (Supplementary Fig. 6). Taken together, in the type III fibril, rather than forming a homodimer per layer as in type I and II fibrils, $A\beta_{42}$ forms a heterotrimer—a hybrid of fold 1′ and fold 2.

The structural difference between fold 1′ of the type III fibril and fold 1 of the type I fibril is induced by cofactor binding at the interface of chains A and B. In the protofilamental interface of the type I fibril, residues L17, F19, L34 and V36 form a tight hydrophobic interface devoid of water and other molecules (Fig. 4c and Extended Data Fig. 7a); in contrast, in the interface of chains A and B of the type III fibril, extra densities of unknown molecules squeeze in the hydrophobic hole mainly composed of the side chains of residues L17, F19 and L34 (Fig. 4c and Extended Data Fig. 7b), which consequently reshape the protofilamental interface and the overall fold of the $A\beta_{42}$ fibril.

To exclude the possibility that the extra densities are sarkosyl molecules introduced during fibril extraction, we extracted fibrils from AD1 brain again using a water-based extraction method without the addition of sarkosyl (Extended Data Fig. 8a,b and Supplementary Table 2). Although the extracted fibrils were not homogeneous enough for high-resolution structure determination, 2D class averages of the fibrils showed the existence of type III fibrils, confirming that type III fibrils are not induced by sarkosyl (Extended Data Fig. 8c,d). In addition, sarkosyl has a negatively charged headgroup, not suitable for adapting to the hydrophobic environment of the interface of chains A and B of the type III fibril. Thus, the extra densities are most likely brain molecules that were incorporated into the type III fibril during fibril formation.

In addition to the structural difference at the interface, chains A and B of the type III fibril also feature distinct modifications at the fibril

https://doi.org/10.1038/s41589-025-01921-4

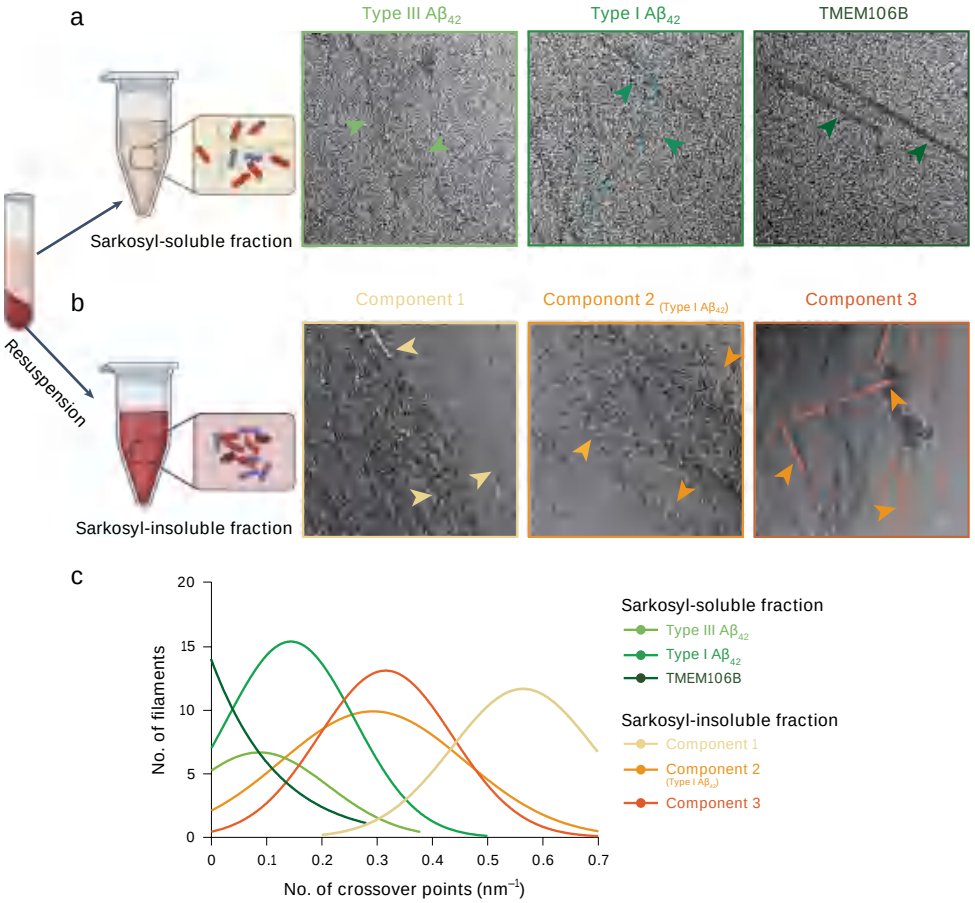

Fig. 3 | Sedimentation and clustering behaviors of fibrils extracted from the AD1 case. a,**b**, Cryo-EM images showing the locations of cryo-EM particles at the fibrils in the soluble (top; **a**) and insoluble (bottom; **b**) fractions. The particles of the fibrils in the soluble fraction and the type I $A\beta_{42}$ fibrils in the insoluble fraction were classified from the first 3D classification. The particles of unidentified components 1 and 3 in the insoluble fraction were classified on the basis of the 2D classification. Particles are shown as dots and those belonging to different types of fibrils are colored differently. The cartoons were created with BioRender.com. **c**, Distribution of crossover points per unit length for each type of fibril. One fibril intersecting with another fibril is counted as one crossover point. For each fibril type, $n = 80$ fibrils. To minimize bias, the micrographs containing at least five fibrils and fibrils with a length > 130 nm were picked. The numbers of crossover points were analyzed by frequency distribution in GraphPad Prism 8.

surface compared to the type I fibril. On the surface of the type I fibril, which was similarly extracted in the soluble fraction of AD1, the extra densities are close to a positively charged surface formed by H14 and K16 (Extended Data Fig. 7a), indicating that the cofactors may contain negatively charged groups. In contrast, on the surface of chains A and B of the type III fibril, extra densities present near an overall neutral surface formed by H14, K16, E22 and D23, in which K16 and E22 further form an electrostatic interaction (Extended Data Fig. 7b). Interestingly, extra densities on this surface only exist in chains A and B but not chain C (Extended Data Fig. 7b). In chain C, K28 forms an electrostatic interaction with the terminal carboxyl group of chain B (Extended Data Fig. 7b), which is the same as the protofilamental interface of the type II $A\beta_{42}$ fibril[14] (Extended Data Fig. 7c).

Type I but not type III $A\beta_{42}$ fibrils feature an interior AV-45-binding channel

Given the multiple polymorphs of $A\beta_{42}$ fibrils in human brains, we wondered whether AV-45 (^{18}F-florbetapir), an Aβ positron emission tomography (PET) tracer approved by the FDA and widely used for AD diagnosis[26], has selective binding to Aβ polymorphic fibrils. We thus sought to investigate the binding mechanism of AV-45 to $A\beta_{42}$ fibrils. We incubated the soluble fraction of the AD1 brain that contained both type I and type III $A\beta_{42}$ fibrils with AV-45 at room temperature for 1 h. We then prepared samples for cryo-EM data collection. The 2D classifications revealed no obvious change in helical parameters upon the addition of AV-45 (Supplementary Table 2 and Extended Data Fig. 9a,b). The 3D reconstructions of type I and type III fibrils in complex with AV-45 (referred to as type I:AV-45 and type III:AV-45, respectively) were determined at overall resolutions of 3.5 Å and 3.7 Å, respectively (Extended Data Fig. 2 and Supplementary Table 2).

Remarkably, in the type I:AV-45 complex, we observed tube-like extra densities located at the head-to-tail interface of the two protofilaments (Fig. 5a,b). These densities did not exist in our type I fibril without AV-45 incubation (Fig. 5a) or in type I fibrils extracted from the insoluble fraction of AD brains reported previously[14,32] (Extended Data Fig. 9c), indicating that the extra densities represent AV-45. We then built the structural model for the type I:AV-45 complex (Fig. 5c). The overall structures of $A\beta_{42}$ in the type I fibril with or without AV-45 were nearly identical (Extended Data Fig. 9d). In contrast, the addition of AV-45 led to its localization in a channel formed by residues 15–17 and 36–39 from the opposing protofilaments (Fig. 5c,d). On the basis of the tube-like densities, we fitted AV-45 parallel to the fibril axis (Fig. 5d), indicating a vertical binding geometry of AV-45 to the type I $A\beta_{42}$ fibril[34].

In contrast to the type I:AV-45 complex, we did not observe additional extra densities in the type III:AV-45 complex maps (Extended Data Fig. 9e,f) nor did we observe any structural change of the type III fibril upon the addition of AV-45 (Extended Data Fig. 9g). Indeed, the type III fibril lacks the AV-45-binding channel seen in the type I fibril (Fig. 5e).

https://doi.org/10.1038/s41589-025-01921-4

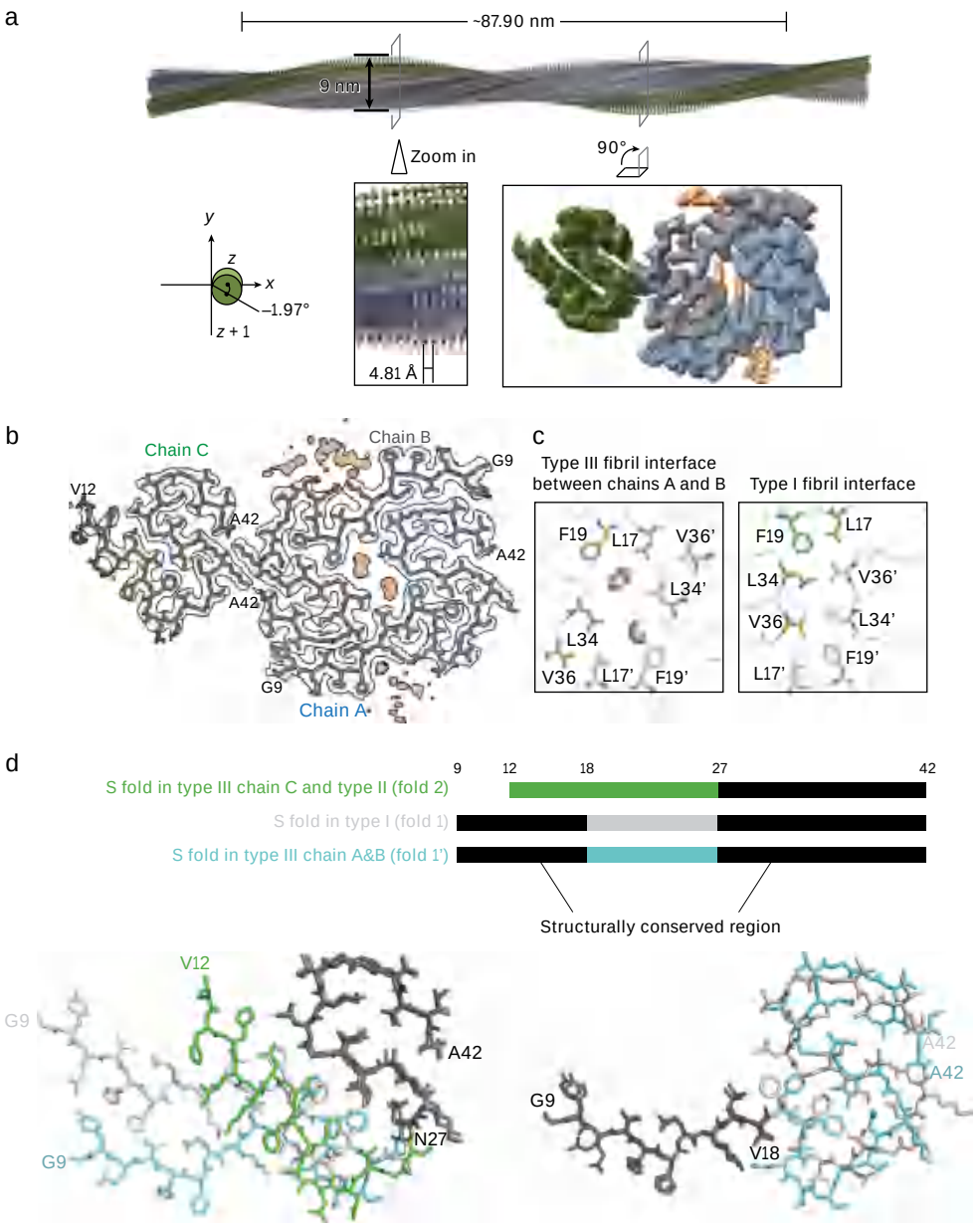

Fig. 4 | Cryo-EM structure of the type III $A\beta_{42}$ fibril. a, Cryo-EM density map of the type III $A\beta_{42}$ fibril with three protofilaments colored differently. The map of one crossover (360° helical turn) is shown, with a zoomed-in side view and cross-section view. The fibril width, twist angle and rise are indicated. Extra densities are colored in orange. **b**, Structural model of type III $A\beta_{42}$ fibril fitted in its density map. The density map is restricted to areas within a 2-Å radius of the structural model. **c**, Structural comparison of the S-shaped folds in $A\beta_{42}$ fibril structures. Top, schematic depicting the conformational conserved regions in fold 1 and fold 1′ (9–18 and 27–42; black) and variable regions in different folds. Bottom left, overlay of fold 1, fold 1′ and fold 2 based on structural similarities of residues 27–42 (gray; fold 2 versus fold 1 and fold 1′, r.m.s.d. of 0.939 Å over 16 Cα atoms and 0.979 Å over 16 Cα atoms). Bottom right, overlay of the structures of fold 1 and fold 1′ on the basis of structural similarities of residues 9–18 (gray; r.m.s.d. of 0.480 Å over ten Cα atoms). **d**, Protofilamental interfaces of chains A and B of type III $A\beta_{42}$ fibril (left) and type I $A\beta_{42}$ fibril (right). Extra densities are colored in orange.

Although the head-to-tail interface is also present in the type III fibril, the binding of native cofactors in the protofilamental interface results in a 10.2-Å sliding of the head-to-tail interface, which consequently closes the AV-45-binding channel (Fig. 5e). Thus, these data indicate that the type I $A\beta_{42}$ fibril, which is widely present in sporadic AD brains, accommodates AV-45 with a unique interior channel, whereas this channel does not exist in type III.

To further investigate the binding of AV-45 to type I and type III $A\beta_{42}$ fibrils, we stained the brain slices of AD1, which contained both types, with Aβ antibody immunostaining and AV-45 fluorescence (Supplementary Fig. 7). A gradient concentration of AV-45 from 10 μM to 1 μM was applied. The result showed a good match of AV-45 and Aβ antibody in staining different morphologies of Aβ plaques, including the so-called dense plaques and focal deposits[35] (Supplementary Fig. 7). In addition, as the concentration of AV-45 decreased, its fluorescence faded in line with the density of Aβ plaques (Supplementary Fig. 7). Thus, although the type III $A\beta_{42}$ fibril does not contain the interior channel seen in type I, whether it can bind to AV-45 in a manner different from type I is unclear. Future assembly of pure type III fibril $A\beta_{42}$ may clarify this point.

Discussion

The sarkosyl-based purification method has been widely used in the extraction of endogenous amyloid fibrils. The ultracentrifugal supernatant (referred to as soluble fraction in this work) was previously

https://doi.org/10.1038/s41589-025-01921-4

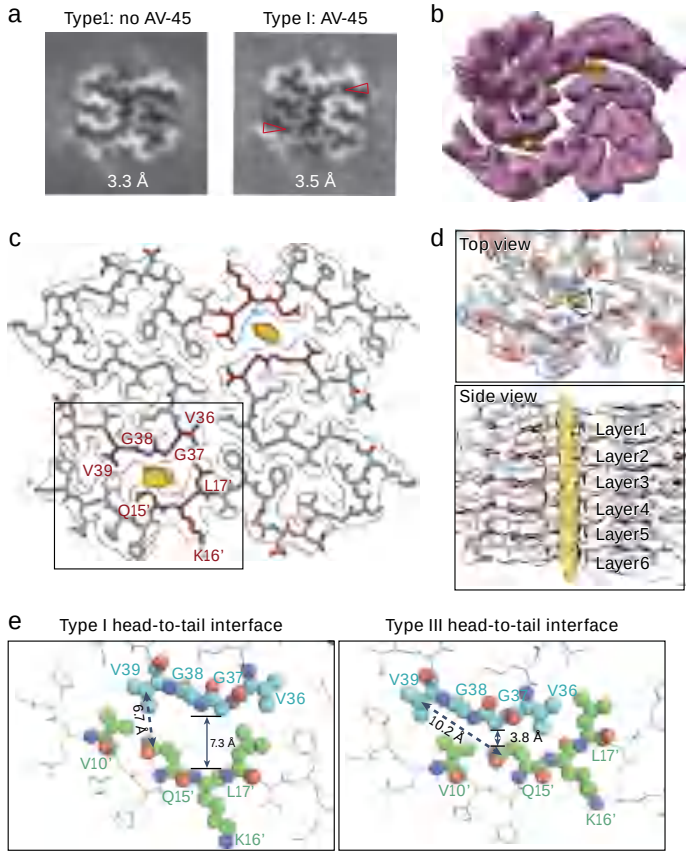

Fig. 5 | AV-45 binds to an interior channel of the type I $A\beta_{42}$ fibril. a, Central slices of cryo-EM 3D maps of the soluble type I fibril with and without the addition of AV-45. Red hollow arrowheads indicate the extra densities. **b**, Reconstructed density map of type I:AV-45 complex. Aβ densities are in purple; extra densities of AV-45 are in orange. **c**, Structural model of type I:AV-45 fitted in the density map. The density map is restricted to the area within a 2-Å radius of the structural model. Extra densities are colored in orange. The AV-45-binding channel is framed out and the residues forming the channel are labeled and highlighted in dark red. **d**, Top and side views of the AV-45-binding channel with the AV-45 structure fitted in the map. **e**, Protofilamental head-to-tail interfaces of type I (left) and type III (right) $A\beta_{42}$ fibrils. Residues composing the AV-45-binding channel are labeled and shown in spheres. The size of the channel and the distance between Q15 and V39 from the opposing protofilaments are indicated.

considered to be soluble amyloid oligomers or protofibrils. However, a recent study showed abundant Aβ fibrils in the soluble fraction of AD brains, which exhibited the same structures as the Aβ fibrils in the insoluble fraction[32]. In our study, we also observed abundant amyloid fibrils, including $A\beta_{42}$ and TMEM106B fibrils, in the soluble fractions of AD brains. More importantly, we found a new type (type III) of $A\beta_{42}$ fibril that appears as a hybrid of types I and II and is exclusively present in the soluble fraction of one AD brain (case AD1). Because type I and II $A\beta_{42}$ fibrils are stable in sarkosyl[14], type III is less likely a purification artifact and more likely formed in the special context of AD1. Unfortunately, we have only one example of the type III fibril because of limited brain samples. If more cases were included, especially cases with similar disease conditions to AD1, it could be clarified which disease subtype contains the type III $A\beta_{42}$ fibril. Nevertheless, our work shows different $A\beta_{42}$ fibril strains in different persons with AD. Although all participants were clinically and neurologically diagnosed as having AD, each individual may feature a special pathological environment that generates distinctive cofactors modifying amyloid fibril formation. Different amyloid fibril strains may further lead to disease heterogeneity, which on the other hand may contribute to precise classification of AD subtypes[36,37].

Chemical modifications are determinant factors for the formation of polymorphic amyloid fibrils[38,39]. Indeed, formation of the type III $A\beta_{42}$ fibril is induced by cofactor binding at the interface of Aβ chains. Similar extra densities were also observed in the ex vivo Aβ fibrils extracted from the tg-APP_{ArcSwe} mouse model (Extended Data Fig. 10a,b). However, this murine Aβ fibril composed of two protofilaments is structurally more similar to the AD type I fibril (Extended Data Fig. 10c,d)[40]. Furthermore, we argue that, even with the same atomic structures, the fibrils in the soluble and insoluble fractions may carry various surface modifications, which endow fibrils with distinct physicochemical properties. This may explain why the same fibril structure (for example, type I $A\beta_{42}$ fibril) exhibits different sedimentation properties (existing in both soluble and insoluble fractions).

PET imaging of Aβ aggregates has been widely used for diagnosing AD, assessing disease progression and monitoring the effects of clinical trials[12,26,41–44]. Currently several Aβ PET tracers have been approved for clinical use, such as AV-45 (refs. 26,45,46), ^{18}F-florbetaben[47,48] and ^{18}F-flutemetamol[49–51]. However, the mechanism of how PET tracers recognize Aβ fibrils is unclear, which hampers rational design and optimization for Aβ-specific tracers. In this study, we investigated the mechanism of AV-45 binding to type I and type III $A\beta_{42}$ fibrils, which are the two types found by far in sporadic AD brains. Our work revealed that, unlike the previously reported amyloid-binding ligands that normally decorate the fibril surface[25,34,52–54], AV-45 remarkably inserts into an interior channel of the type I $A\beta_{42}$ fibril. This observation enriches our mechanistic understanding of the ligand binding to amyloid fibrils and also provides new insight into the potential ligand-binding site of amyloid fibrils.

Online content

Any methods, additional references, Nature Portfolio reporting summaries, source data, extended data, supplementary information, acknowledgements, peer review information; details of author contributions and competing interests; and statements of data and code availability are available at https://doi.org/10.1038/s41589-025-01921-4.

References

1. Goedert, M. & Spillantini, M. G. A century of Alzheimer's disease. *Science* **314**, 777–781 (2006).
2. McKhann, G. et al. Clinical diagnosis of Alzheimer's disease: report of the NINCDS–ADRDA Work Group under the auspices of Department of Health and Human Services Task Force on Alzheimer's Disease. *Neurology* **34**, 939–944 (1984).
3. Knopman, D. S. et al. Alzheimer disease. *Nat. Rev. Dis. Prim.* **7**, 33 (2021).
4. Long, J. M. & Holtzman, D. M. Alzheimer disease: an update on pathobiology and treatment strategies. *Cell* **179**, 312–339 (2019).
5. Braak, H. & Braak, E. Neuropathological stageing of Alzheimer-related changes. *Acta Neuropathol.* **82**, 239–259 (1991).
6. Chiti, F. & Dobson, C. M. Protein misfolding, amyloid formation, and human disease: a summary of progress over the last decade. *Annu. Rev. Biochem.* **86**, 27–68 (2017).
7. Hardy, J. & Selkoe, D. J. The amyloid hypothesis of Alzheimer's disease: progress and problems on the road to therapeutics. *Science* **297**, 353–356 (2002).
8. McKhann, G. M. et al. The diagnosis of dementia due to Alzheimer's disease: recommendations from the National Institute on Aging–Alzheimer's Association workgroups on diagnostic guidelines for Alzheimer's disease. *Alzheimers Dement.* **7**, 263–269 (2011).
9. McDonald, C. Clinical heterogeneity in senile dementia. *Br. J. Psychiatry* **115**, 267–271 (1969).
10. Haxby, J. V., Duara, R., Grady, C. L., Cutler, N. R. & Rapoport, S. I. Relations between neuropsychological and cerebral metabolic asymmetries in early Alzheimer's disease. *J. Cereb. Blood Flow. Metab.* **5**, 193–200 (1985).

11. Duara, R. et al. Positron emission tomography in Alzheimer's disease. *Neurology* **36**, 879–887 (1986).
12. Vogel, J. W. et al. Four distinct trajectories of Tau deposition identified in Alzheimer's disease. *Nat. Med.* **27**, 871–881 (2021).
13. Gilbert, M. A. G. et al. CryoET of β-amyloid and Tau within postmortem Alzheimer's disease brain. *Nature* **631**, 913–919 (2024).
14. Yang, Y. et al. Cryo-EM structures of amyloid-β 42 filaments from human brains. *Science* **375**, 167–172 (2022).
15. Yang, Y. et al. Cryo-EM structures of amyloid-β filaments with the Arctic mutation (E22G) from human and mouse brains. *Acta Neuropathol.* **145**, 325–333 (2023).
16. Fernandez, A. et al. Cryo-EM structures of amyloid-β and Tau filaments in Down syndrome. *Nat. Struct. Mol. Biol.* **31**, 903–909 (2024).
17. Lu, J. X. et al. Molecular structure of β-amyloid fibrils in Alzheimer's disease brain tissue. *Cell* **154**, 1257–1268 (2013).
18. Qiang, W., Yau, W. M., Lu, J. X., Collinge, J. & Tycko, R. Structural variation in amyloid-beta fibrils from Alzheimer's disease clinical subtypes. *Nature* **541**, 217–221 (2017).
19. Ghosh, U., Thurber, K. R., Yau, W. M. & Tycko, R. Molecular structure of a prevalent amyloid-beta fibril polymorph from Alzheimer's disease brain tissue. *Proc. Natl Acad. Sci. USA* **118**, e2023089118 (2021).
20. Lee, M., Yau, W. M., Louis, J. M. & Tycko, R. Structures of brain-derived 42-residue amyloid-β fibril polymorphs with unusual molecular conformations and intermolecular interactions. *Proc. Natl Acad. Sci. USA* **120**, e2218831120 (2023).
21. Fitzpatrick, A. W. P. et al. Cryo-EM structures of Tau filaments from Alzheimer's disease. *Nature* **547**, 185–190 (2017).
22. Yang, Y. et al. Structures of α-synuclein filaments from human brains with Lewy pathology. *Nature* **610**, 791–795 (2022).
23. Bennett, R. E. et al. Enhanced Tau aggregation in the presence of amyloid β. *Am. J. Pathol.* **187**, 1601–1612 (2017).
24. de Calignon, A. et al. Propagation of Tau pathology in a model of early Alzheimer's disease. *Neuron* **73**, 685–697 (2012).
25. Shi, Y., Ghetti, B., Goedert, M. & Scheres, S. H. W. Cryo-EM structures of chronic traumatic encephalopathy Tau filaments with PET ligand flortaucipir. *J. Mol. Biol.* **435**, 168025 (2023).
26. Clark, C. M. et al. Use of florbetapir-PET for imaging β-amyloid pathology. *JAMA* **305**, 275–283 (2011).
27. Schweighauser, M. et al. Age-dependent formation of TMEM106B amyloid filaments in human brains. *Nature* **605**, 310–314 (2022).
28. Chang, A. et al. Homotypic fibrillization of TMEM106B across diverse neurodegenerative diseases. *Cell* **185**, 1346–1355 (2022).
29. Jiang, Y. X. et al. Amyloid fibrils in disease FTLD-TDP are composed of TMEM106B not TDP-43. *Nature* **605**, 304–309 (2022).
30. Fan, Y. et al. Generic amyloid fibrillation of TMEM106B in patient with Parkinson's disease dementia and normal elders. *Cell Res.* **32**, 585–588 (2022).
31. Vicente, C. T. et al. C-terminal TMEM106B fragments in human brain correlate with disease-associated TMEM106B haplotypes. *Brain* **146**, 4055–4064 (2023).
32. Stern, A. M. et al. Abundant Aβ fibrils in ultracentrifugal supernatants of aqueous extracts from Alzheimer's disease brains. *Neuron* **111**, 2012–2020 (2023).
33. Radamaker, L. et al. Cryo-EM reveals structural breaks in a patient-derived amyloid fibril from systemic AL amyloidosis. *Nat. Commun.* **12**, 875 (2021).
34. Tao, Y. et al. Structural mechanism for specific binding of chemical compounds to amyloid fibrils. *Nat. Chem. Biol.* **19**, 1235–1245 (2023).
35. Yamaguchi, H., Hirai, S., Morimatsu, M., Shoji, M. & Ihara, Y. A variety of cerebral amyloid deposits in the brains of the Alzheimer-type dementia demonstrated by β protein immunostaining. *Acta Neuropathol.* **76**, 541–549 (1988).
36. Li, D. & Liu, C. Conformational strains of pathogenic amyloid proteins in neurodegenerative diseases. *Nat. Rev. Neurosci.* **23**, 523–534 (2022).
37. Soto, C. & Pritzkow, S. Protein misfolding, aggregation, and conformational strains in neurodegenerative diseases. *Nat. Neurosci.* **21**, 1332–1340 (2018).
38. Li, D. & Liu, C. Hierarchical chemical determination of amyloid polymorphs in neurodegenerative disease. *Nat. Chem. Biol.* **17**, 237–245 (2021).
39. Zhao, K. et al. Parkinson's disease-related phosphorylation at Tyr39 rearranges α-synuclein amyloid fibril structure revealed by cryo-EM. *Proc. Natl Acad. Sci. USA* **117**, 20305–20315 (2020).
40. Zielinski, M. et al. Cryo-EM of Aβ fibrils from mouse models find tg-APP(ArcSwe) fibrils resemble those found in patients with sporadic Alzheimer's disease. *Nat. Neurosci.* **26**, 2073–2080 (2023).
41. de Wilde, A. et al. Association of amyloid positron emission tomography with changes in diagnosis and patient treatment in an unselected memory clinic cohort: yhe ABIDE project. *JAMA Neurol.* **75**, 1062–1070 (2018).
42. van Dyck, C. H. et al. Lecanemab in early Alzheimer's disease. *N. Engl. J. Med.* **388**, 9–21 (2023).
43. Wolk, D. A. et al. Association between in vivo fluorine 18-labeled flutemetamol amyloid positron emission tomography imaging and in vivo cerebral cortical histopathology. *Arch. Neurol.* **68**, 1398–1403 (2011).
44. Ossenkoppele, R. et al. Amyloid and Tau PET-positive cognitively unimpaired individuals are at high risk for future cognitive decline. *Nat. Med.* **28**, 2381–2387 (2022).
45. Salloway, S. et al. Amyloid positron emission tomography and cerebrospinal fluid results from a crenezumab anti-amyloid-β antibody double-blind, placebo-controlled, randomized phase II study in mild-to-moderate Alzheimer's disease (BLAZE). *Alzheimers Res. Ther.* **10**, 96 (2018).
46. Johnson, K. A. et al. Florbetapir (F18-AV-45) PET to assess amyloid burden in Alzheimer's disease dementia, mild cognitive impairment, and normal aging. *Alzheimers Dement.* **9**, S72–S83 (2013).
47. Sabri, O. et al. Florbetaben PET imaging to detect amyloid β plaques in Alzheimer's disease: phase 3 study. *Alzheimers Dement.* **11**, 964–974 (2015).
48. Barthel, H. et al. Cerebral amyloid-β PET with florbetaben (^{18}F) in patients with Alzheimer's disease and healthy controls: a multicentre phase 2 diagnostic study. *Lancet Neurol.* **10**, 424–435 (2011).
49. Curtis, C. et al. Phase 3 trial of flutemetamol labeled with radioactive fluorine 18 imaging and neuritic plaque density. *JAMA Neurol.* **72**, 287–294 (2015).
50. Vandenberghe, R. et al. ^{18}F-flutemetamol amyloid imaging in Alzheimer disease and mild cognitive impairment: a phase 2 trial. *Ann. Neurol.* **68**, 319–329 (2010).
51. Duara, R. et al. Amyloid positron emission tomography with ^{18}F-flutemetamol and structural magnetic resonance imaging in the classification of mild cognitive impairment and Alzheimer's disease. *Alzheimers Dement.* **9**, 295–301 (2013).
52. Xiang, J. et al. Development of an α-synuclein positron emission tomography tracer for imaging synucleinopathies. *Cell* **186**, 3350–3367 (2023).
53. Shi, Y. et al. Cryo-EM structures of Tau filaments from Alzheimer's disease with PET ligand APN-1607. *Acta Neuropathol.* **141**, 697–708 (2021).
54. Merz, G. E. et al. Stacked binding of a PET ligand to Alzheimer's Tau paired helical filaments. *Nat. Commun.* **14**, 3048 (2023).

[1]Bio-X Institutes, Key Laboratory for the Genetics of Developmental and Neuropsychiatric Disorders (Ministry of Education), Shanghai Jiao Tong University, Shanghai, China. [2]Zhangjiang Institute for Advanced Study, Shanghai Jiao Tong University, Shanghai, China. [3]Interdisciplinary Research Center on Biology and Chemistry, Shanghai Institute of Organic Chemistry, Chinese Academy of Sciences, Shanghai, China. [4]State Key Laboratory of Chemical Biology, Shanghai Institute of Organic Chemistry, University of Chinese Academy of Sciences, Chinese Academy of Sciences, Shanghai, China. [5]Synthetic and Functional Biomolecules Center, Beijing National Laboratory for Molecular Sciences, Key Laboratory of Bioorganic Chemistry and Molecular Engineering of Ministry of Education, College of Chemistry and Molecular Engineering, Peking University, Beijing, China. [6]Center for Brain Health and Brain Technology, Global Institute of Future Technology, Shanghai Jiao Tong University, Shanghai, China. [7]Department of Neurology, Institute on Aging and Brain Disorders, The First Affiliated Hospital of USTC, Division of Life Sciences and Medicine, University of Science and Technology of China, Hefei, China. [8]Neurodegenerative Disorder Research Center, Anhui Province Key Laboratory of Biomedical Aging Research, Division of Life Sciences and Medicine, University of Science and Technology of China, Hefei, China. [9]Department of Human Anatomy, Histology and Embryology, Institute of Basic Medical Sciences, Neuroscience Center, Chinese Academy of Medical Sciences, School of Basic Medicine, Peking Union Medical College, Beijing, China. [10]Shanghai Academy of Natural Sciences (SANS), Fudan University, Shanghai, China. [11]These authors contributed equally: Qinyue Zhao, Youqi Tao. ✉e-mail: qiuwy73@126.com; liulab@sioc.ac.cn; lidan2017@sjtu.edu.cn

Methods

Postmortem human brain samples

The subjects of this study were three clinically diagnosed AD cases. Ethical approval was obtained from the Institutional Review Board of the Institute of Basic Medical Sciences, Chinese Academy of Medical Sciences (approval numbers 009-2014, 031-2017 and 2022125). All AD brain samples were provided by the National Human Brain Bank for Development and Function, Chinese Academy of Medical Science and Peking Union Medical College. The individual cases were as follows:

AD1: An 83-year-old man diagnosed with progressive dementia, exhibiting parkinsonian symptoms such as muscular hypertonia. Neuropathological examination confirmed severe CAA. The cause of death was cerebral infarction.

AD2: An 84-year-old woman suffering from dementia, additionally diagnosed with an abdominal aortic aneurysm. The cause of death was cardiac failure.

AD3: An 89-year-old man presenting similar parkinsonian behavior to AD1. The cause of death was attributed to Parkinson's respiratory failure.

IHC staining

IHC staining was carried out following a previously described protocol[30]. Briefly, frontal cortex tissues from three persons with AD were postfixed in a 10% paraformaldehyde (PFA) solution, gradient-dehydrated in sucrose and then embedded in paraffin. Then, 6-µm-thick sections were cut and underwent deparaffinization and rehydration.

To enhance staining quality, sections were manually treated with 98% formic acid (FA) for $A\beta_{42}$, $A\beta_{40}$ and TMEM106B staining and with standard machine heat retrieval at 95 °C for 15 min in citrate buffer (pH 6.0) for α-syn staining. The slices were subsequently treated with hydrogen peroxide for 30 min to inhibit endogenous peroxidase activity.

The sections were then incubated in blocking buffer (2% BSA in 0.1 M Tris-HCl pH 7.6) for 5 min, followed by overnight incubation at 4 °C with primary antibodies specific to $A\beta_{42}$ (BioLegend, 812101; 1:250), $A\beta_{40}$ (BioLegend, 867801; 1:1,000), phosphorylated Tau (Thermo Fisher Scientific, MN1020; 1:1,000), α-syn (BioLegend, MMS-5085; 1:250) or TMEM106B (Novus, NBP1-91311; 1:250).

Sections were subsequently incubated with a biotin-conjugated secondary antibody (1:1,000; BA-Vector) for 1 h at 25 °C. Visualization of the antigen was achieved using VECTASTAIN ABC kits (Vector Laboratories, ZJ1115) and ImmPACT DAB substrate kits (Vector Laboratories, ZJ0908A) and sections were finally counterstained with hematoxylin.

MS

Sample preparation. In preparation for the bottom-up proteome sample, the samples were resuspended in a solution containing 8 M urea and 100 mM Tris-HCl at pH 8.0. The proteins were reduced with 10 mM dithiothreitol at 37 °C for 30 min, followed by alkylation with 20 mM iodoacetamide at 35 °C for 30 min. Subsequently, the urea concentration was reduced to 1 M using Tris-HCl at pH 8.0 and the proteins were enzymatically digested with trypsin overnight, with a trypsin concentration of 10 ng μl^{-1}. The trypsin digestion was halted by the addition of FA to achieve a final concentration of 2%. The resulting peptides were purified using custom-made C18 (3M Empore) stage tips and eluted with 200 µl of a solution containing 50% acetonitrile and 0.1% FA.

For the top-down proteome analysis, the samples were reconstituted in 100 µl of hexafluoroisopropanol. Following sonication at 40% amplitude, the fibrils were incubated at 37 °C for 2 h, then centrifuged at 100,000*g* for 15 min and finally dried using vacuum centrifugation. The dried samples were then reconstituted in a solution containing 2% acetonitrile and 2% FA, followed by centrifugation at 13,000 rpm for 5 min. The supernatants were purified using custom-made C18 (3M Empore) stage tips, with peptide elution performed sequentially using 200 µl of 50% acetonitrile in 0.1% FA and then 100% acetonitrile.

LC–MS/MS analysis. The samples were resuspended with of solvent A (0.1% FA in H_2O) and loaded on an in-house prepared silica column (15 cm × 100 µm, C18 1.9 µm) using an Ultimate 3000 LC system. The peptides were eluted by a linear gradient from 5% to 40% solvent B (solvent A, 0.1% FA in H_2O; solvent B, 0.1% FA in acetonitrile) in 120 min. The eluted peptides were analyzed by a Q-Exactive Orbitrap MS instrument (Thermo Fisher Scientific), with full mass scan from 350 to 1,800 m/z. MS/MS fragmentation was performed in a data-dependent mode, with which the 20 most intense ions were selected for MS/MS analysis. Full mass resolution was set as 70,000 and MS/MS resolution was set as 17,500. The normalized collision energy was 28%, full mass maximum ion transfer time was 50 ms and MS/MS maximum ion transfer time was 45 ms. The dynamic exclusion time was set as 23 s.

Database search. The raw files were searched against the sequence of human A4 proteins released from UniProt by pFind. For the bottom-up experiment, three missed cleavages by trypsin was allowed. For the top-down experiment, no enzymatic digestion was set. Cysteine carbamidomethyl was set as a fixed modification, whereas the oxidation of methionine was a variable modification. Cysteine carbamidomethyl was set as a fixed modification, whereas the oxidation of methionine was a variable modification. Open search was selected to take consideration of all modifications in Unimod as candidate modifications in our data. The tolerance of both precursor and fragment ions was set to 20 ppm. A peptide length ≥ 7 aa was included. In each search engine dataset, the global false discovery rate was set as ≤1% in the peptide spectrum match, peptide and protein levels.

Western blot

The sarkosyl-soluble fibrils of AD1 were suspended in SDS–PAGE loading dye, sonicated for 40 cycles (1 s on and off per cycle) under 20% amplitude (JY92-IIN sonicator), boiled for 10 min and loaded on 4–20% Bis–Tris gels (GenScript), followed by electrophoresis at 140 V for 40 min. Western blotting was performed as previously described[55]. Primary antibodies were rabbit monoclonal antibody specific to $A\beta_{1-42}$ (1:2,000; BioLegend) and mouse monoclonal antibody specific to $A\beta_{1-16}$ (1:2,000; BioLegend).

Immunofluorescence and AV-45 staining

Immunofluorescence and AV-45 staining was performed according to the protocol previously reported[56]. Briefly, postmortem brain tissue of AD1 was fixed in 4% PFA, followed by gradient dehydration in 20% and 30% sucrose solution. Next, the brain tissue was embedded in optimal cutting temperature (OCT) compound (4583, Sakura) and cut into 12-µm-thick sections with a cryotome. Brain sections were washed with PBS for 10 min at room temperature to remove OCT. After permeabilization using PBS containing 0.5% Triton X-100 for 10 min, sections were incubated with 3% Sudan black for 10 min. Following two washing steps with 70% ethanol, brain sections used for fluorescence labeling with AV-45 were incubated in 30% ethanol containing 10 µM (or a concentration gradient from 10 to 5, 3 and 1 µM) at room temperature for 2 h. Then, the sections were incubated with 5% BSA for blocking after 30% ethanol washing for 2 min. As for the immunostaining, primary antibody to Aβ (6E10, BioLegend) was applied to brain slices and incubated at room temperature for 2 h, followed by incubation with secondary fluorescence antibodies (Alexa Fluor 594-coupled goat anti-mouse IgG from Invitrogen, Thermo Fisher Scientific; 1:1,000) at room temperature for 1 h and washing three times with PBS. After a final wash, the samples were dipped into distilled water for 5 min and mounted in nonfluorescent mounting medium (0100-01, SouthernBiotech). Sections were scanned with a lightsheet confocal microscope.

Amyloid fibril extraction

The extraction of amyloid fibrils from postmortem frozen brain tissues of persons with AD was performed as previously reported with

moderate modification[14,30]. In brief, frozen frontal cortex tissues were manually homogenized three times in 20 volumes (v/w) of extraction buffer, containing 10 mM Tris-HCl pH 7.5, 0.8 M NaCl, 10% sucrose, 1 mM EGTA, 0.1% sarkosyl, 0.2 M PMSF and protease inhibitor cocktail (Roche). Homogenates were brought to 2% sarkosyl and incubated at 37 °C for 1 h while constantly mixing with a rotary mixer, followed by centrifugation at 10,000*g* for 10 min at 4 °C. The supernatants were subjected to ultracentrifugation at 100,000*g* with SW41Ti (Beckman Coulter) for 60 min at 4 °C yielding both sarkosyl-soluble and sarkosyl-insoluble fractions. The sarkosyl-insoluble fraction was further resuspended with extraction buffer (1,000 µl g^{-1} tissue) followed by low-speed centrifugation at 3,000*g* for 5 min at 4 °C; the supernatants were diluted threefold with buffer consisting of 50 mM Tris-HCl pH 7.5, 0.15 M NaCl, 10% sucrose and 0.2% sarkosyl and centrifuged at 166,000*g* with TLA100.3 (Beckman Coulter) for 1 h at 4 °C. Similarly, the sarkosyl-soluble fraction was also performed 166,000*g* centrifugation with TLA100.3 (Beckman Coulter) for 1 h at 4 °C. The pellets in two fractions were resuspended with 20 mM Tris-HCl pH 7.4 and 50 mM NaCl (100 µl g^{-1} tissue). For NS-TEM and cryo-EM applications, pellets from the soluble and insoluble fractions were treated with 0.4 mg ml^{-1} pronase for 1 h to digest amorphous aggregates and remove the fuzzy coat surrounding the amyloid fibrils.

For water-based extraction method, brain tissues were extracted using ice-cold water following a previously described protocol[57]. In brief, 1 g of brain tissues were cut with a scalpel into cubes of less than 1 mm^3 and washed four times with 500 µl of Tris-Ca buffer (20 mM Tris-HCl pH 8.0, 138 mM NaCl, 2 mM $CaCl_2$ and 0.1% w/v NaN_3) at 4 °C. Following each wash, the samples were centrifuged at 3,000*g* for 1 min, with a 5-min spin at 12,000*g* after the final wash. The pellets were then incubated overnight with 5 mg ml^{-1} collagenase from *Clostridium histolyticum* (Sigma-Aldrich) in 1 ml of Tris-Ca buffer at 37 °C. Following a 5-min centrifugation at 12,000*g* at 4 °C, they were washed five times with 500 µl of 50 mM Tris-HCl pH 7.4 and 10 mM EDTA, with a 5-min centrifugation at 12,000*g* after each wash. To collect Aβ fibrils, 100 µl of cold water was added to the pellet, followed by a 5-min centrifugation at 12,000*g*. This step was repeated 12 times. The supernatants of the last four washed were combined and centrifuged at 166,000*g* for 1 h. The pellet was resuspended in 100 µl g^{-1} 20 mM Tris-HCl pH 7.4 and 50 mM NaCl and used for subsequent cryo-EM analysis.

NS-TEM and immunogold NS-TEM

An aliquot of 3 µl of brain-extracted sample was applied to glow-discharged 230-mesh carbon-coated copper grids (Beijing Zhongjingkeyi Technology). After 45-s incubation, the excess sample was blotted away with filter paper and the grid was sequentially washed with 5 µl of double-distilled H_2O and 5 µl of 2% w/v uranyl acetate. The sample-containing grid was stained with another 5 µl of 2% w/v uranyl acetate for 45 s and dried in air before acquiring TEM images. Grid was assessed by using Tecnai G2 spirit TEM instrument with 120-kV voltage (FEI) equipped with a 4,000 × 4,000 charged-coupled device camera (BM-Eagle, FEI Tecnai).

For immunogold NS-TEM, 5 µl of sarkosyl-soluble brain-extracted fibrils were loaded onto the glow-discharged 230-mesh carbon-coated copper grids and incubated for 10 min. The grids were blocked with 0.1% BSA for 30 min at room temperature, followed by incubation with primary antibodies, including anti-$Aβ_{1–16}$ (6E10, BioLegend) and anti-$Aβ_{42}$ (12F4, BioLegend), at 1:15 for 30 min at room temperature. After washing three times with PBS, the grids were incubated with immunogold-labeled secondary antibodies, including anti-rabbit antibody labeled with 12 nm of colloidal gold (1:15; 711-205-152, Jackson ImmunoResearch) for samples stained with anti-$Aβ_{42}$ antibodies and anti-mouse antibody labeled with 12 nm of colloidal gold (1:15; 115-195-146, Jackson ImmunoResearch) for samples stained with anti-$Aβ_{1–16}$ antibody for 30 min at room temperature. After sequentially washing with PBS, double-distilled H_2O and 2% w/v uranyl acetate, the grids were stained with 2% w/v uranyl acetate for 45 s. Then, the excess buffer was removed with filter paper. The TEM micrographs were collected on a Tecnai T12 microscope (FEI) operated at 120 kV.

Atomic force microscopy (AFM)

To characterize the chirality of the newly identified type III Aβ fibril, 2 µl of a tenfold diluted AD1 soluble sample was applied to freshly cleaved mica and settled for 3 min. Afterward, the sample was gently rinsed with Milli-Q water to remove unbound fibrils. The sample was air-dried. Images were acquired using TappingMode on a FastScan Bio AFM system (Bruker). The SNL-10 probe, with a spring constant of 0.35 N m^{-1} was used for scanning. Images were captured at a resolution of 512 × 512 pixels with a line rate at 1.5 Hz. The helical parameters and chirality of fibrils were processed and analyzed using NanoScope Analysis software (version 1.5).

Cryo-EM sample preparation and data collection

After treating with pronase, the 4-µl aliquot of fibril-containing solution was applied to a glow-discharged holey carbon-coated grid (C-Flat, 300-mesh, 1.2/1.3; 71159) and blotted with filter paper after an incubation time of 8 s at 16 °C and 100% humidity. Then, the cryo-EM grids were plunge-frozen in liquid ethane using Vitrobot Mark IV (FEI, Thermo Fisher Scientific).

For image acquisition, the samples were imaged with a Thermo Fisher Titan Krios G4 cryo-TEM instrument (Thermo Fisher Scientific) at 300 kV, equipped with a BioContinuum K3 direct detector (Gatan) in counting mode. A GIF Quantum energy filter (Gatan), with a slit width of 20 eV, was used to remove inelastically scattered electrons. The super-resolution videos were recorded at ×105,000 magnification, with a pixel size of 0.83 Å per pixel and a total dose of ~55 e^- per $Å^2$ over an exposure time of 2.0 s. Automated cryo-EM data collection was performed using EPU software (Thermo Fisher Scientific), with defocus values ranging from −1.0 to −2.4 µm.

Image preprocessing and helical reconstruction

For image preprocessing, the 40 video frames per micrograph were managed using MotionCorr2 to correct for beam-induced motion, align, dose-weight and further bin with a physical pixel size of 0.83 Å (ref. 58). The contrast transfer function (CTF) was estimated from the corrected images using CTFFIND 4.1.8 (ref. 59) and helical reconstruction was performed in RELION 4.0 (refs. 60,61).

Soluble fraction datasets (including AD1 with and without AV-45, AD2 and AD3). Fibrils were manually picked using the 'manual picking' program in RELION 4.0 and individually extracted to segments with a box size of 288 pixels, with an interbox distance of 23.9 Å. These were then re-extracted the particle with a box size of 1,050 and downscaled to 448 pixels. Different polymorphs segments were separated by the reference-free 2D classification steps with a decreasing in-plane angular sampling rate (2°, 0.5° and 0.1°), a descending offset search range (10 pixels, 5 pixels and 3 pixels) and step size (1 pixel, 0.5 pixels and 0.1 pixels) at a $T = 2$ regularization parameter. Segments contributing suboptimal 2D class averages were discarded. The apparent half pitches and initial twist angles were calculated. Segments contributing suboptimal 2D class averages were discarded and the apparent helical parameters were calculated.

For type I and type III $Aβ_{42}$ fibrils, segments encompassing entire helical crossovers were used to construct 3D initial models de novo through the relion_helix_inimodel2d program[62]. The segments that belong to each fibrillar component were selected and re-extracted using a smaller box size of 288 pixels with an interbox distance of 23.9 Å. The re-extracted segments and an initial 3D model that was low-pass-filtered to 60 Å were further applied to perform 3D classifications ($k = 3$) using the helical parameters calculated through the splicing of 2D class averages. The class of segments that yielded the clearest 3D

reconstruction map was selected and subjected to additional rounds of 3D classifications ($k = 1$) with local optimization of helical twist and rise by manually controlling the tau2_fudge factor and healpix_order. Then, 3D autorefinements with optimization of helical twist and rise after reconstructions were carried out. To further improve the resolution of 3D reconstruction maps, we performed Bayesian polishing and CTF refinement, followed by 3D autorefinement. For type III $A\beta_{42}$ fibrils, to further improve the resolution, a new algorithm in RELION 5.0 named 'blush regularization' was adopted in the last run of 3D autorefinement[63]. Finally, the maps were sharpened with a soft-edge solvent mask using the standard 'postprocessing' program in RELION 4.0 (for type I $A\beta_{42}$ fibrils) and RELION 5.0 (for type III $A\beta_{42}$ fibrils)[63,64]. Overall resolution estimates were calculated on the basis of the gold-standard 0.143 Fourier shell correlation (FSC) between the two independently refined half-maps. Local resolution was estimated using the 'local resolution' procedure in RELION 4.0 with the same mask and *B* factor in postprocessing[60].

For type 3 TMEM106B, maps from previous work (EMD-33055) served as the initial model, 60 Å low-pass-filtered to avoid bias[30]. The TMEM106B-like segments were selected and re-extracted using a moderately smaller box size of 512 with an interbox diameter of 42.5 Å. A similar 3D classification ($k = 3$) was performed; the segments from the clearest map were selected and further re-extracted into a much smaller box size of 360 pixels. Then, the best 3D class was used as the initial model for 3D classification ($k = 1$) with an interbox diameter of 29.9 Å. A similar strategy was applied to generate the final map.

Insoluble fraction datasets for AD1 case. For the sarkosyl-insoluble fraction datasets specific to the AD1 case, fibrils were manually picked using the 'manual picking' program in RELION 4.0 and individually extracted to segments with a box size of 196 pixels and an interbox distance of 16.3 Å. The processing followed the same procedures as with the sarkosyl-soluble fraction datasets. However, because of the limited number and featureless segments present in this case, only 3D classification and helical reconstruction were performed specifically for the type I $A\beta_{42}$ fibril.

Analysis of the origin of the fibril particles in the cryo-EM micrographs. The locations of particles that were classified into various polymorphs were mapped back to the original cryo-EM micrographs using a method as previously reported[33]. To minimize bias, only the micrographs containing at least five fibrils, each with a length exceeding 130 nm, were selected for analysis. A total of 80 fibrils were analyzed for each polymorph and the number of cross-points was assessed through frequency distribution analysis using GraphPad Prism 8 software.

Structural model building and refinement

The high quality of the type I fibril in the soluble fraction of cases AD1–AD3 and type III fibril of case AD1 allowed unambiguous assignment of the residues and building the atomic models.

The starting model of type I $A\beta_{42}$ fibrils of the three AD cases was based on the structure of the type I $A\beta_{42}$ fibril (Protein Data Bank (PDB) 7Q4B)[14]. For type III $A\beta_{42}$ and type III:AV-45 fibrils, initial model building was based on previously reported S-shaped folds in type I (PDB 7Q4B) and type II (PDB 7Q4M) protofilaments[14]. The starting three layer coordinates of the fibril core were manually fit into the central region of the sharpened density map in UCSF Chimera 1.13.1 (ref. 65), followed by manual adjustment of the three-layer protein model in WinCoot 0.8.9.2 (ref. 66) and refinement against the corresponding map using the phenix.real_space_refine program in PHENIX 1.13 with secondary-structure and geometry restraints[67]. Both models were validated by the 'comprehensive validation' procedure in PHENIX 1.13 (ref. 67). The resolutions of the models against the final density map and two independently refined half-maps were confirmed on basis of the 0.5 FSC criterion. Statistics for the helical reconstruction and final models are shown in Supplementary Table 2.

For type I:AV-45, the coordinates and geometry restrains of AV-45 were generated using the SMILES string in phenix.elbow[67], followed by manual docking of the ligand into the central region of the sharpened density map using Chimera 1.13.1 (ref. 65). Meanwhile, the models of $A\beta_{42}$ were manually adjusted in WinCoot 0.8.9.2 (ref. 66) and refined against the corresponding map using the phenix.real_space_refine program in PHENIX 1.13 with rotamer, Ramachandran and geometry restraints[67]. Additional details are available in Supplementary Table 2.

Reporting summary

Further information on research design is available in the Nature Portfolio Reporting Summary linked to this article.

Data availability

The cryo-EM maps were deposited to the EM Data Bank (EMDB) under accession numbers EMD-37170 for the AD1 type I $A\beta_{42}$ fibril of soluble fraction, EMD-37197 for the AD1 type III $A\beta_{42}$ fibril of soluble fraction, EMD-37195 for the type I:AV-45 complex, EMD-37200 for the type III:AV-45 complex, EMD-37198 for the AD2 type I $A\beta_{42}$ fibril of soluble fraction and EMD-37199 for the AD3 type I $A\beta_{42}$ fibril of soluble fraction. The corresponding refined atomic models of the AD1 type I, AD3 type III $A\beta_{42}$, type I:AV-45, type III:AV-45, AD2 type I and AD3 type I fibrils were deposited to the PDB under accession numbers 8KEW, 8KF3, 8KF1, 8KF6, 8KF4 and 8KF5, respectively. The density maps used are available from the EMDB under accession number EMD-33055 (type 3 TMEM106B fibril). The structural models used in this study are available from the PDB under accession codes 7Q4B (type I $A\beta_{42}$ fibril) and 7Q4M (type II $A\beta_{42}$ fibril).

References

55. Liu, Z. et al. Hsp27 chaperones FUS phase separation under the modulation of stress-induced phosphorylation. *Nat. Struct. Mol. Biol.* **27**, 363–372 (2020).
56. Zhao, Q. et al. A Tau PET tracer PBB3 binds to TMEM106B amyloid fibril in brain. *Cell Discov.* **10**, 50 (2024).
57. Yang, Y. et al. Cryo-EM structures of Aβ40 filaments from the leptomeninges of individuals with Alzheimer's disease and cerebral amyloid angiopathy. *Acta Neuropathol. Commun.* **11**, 191 (2023).
58. Zheng, S. Q. et al. MotionCor2: anisotropic correction of beam-induced motion for improved cryo-electron microscopy. *Nat. Methods* **14**, 331–332 (2017).
59. Rohou, A. & Grigorieff, N. CTFFIND4: fast and accurate defocus estimation from electron micrographs. *J. Struct. Biol.* **192**, 216–221 (2015).
60. He, S. & Scheres, S. H. W. Helical reconstruction in RELION. *J. Struct. Biol.* **198**, 163–176 (2017).
61. Lovestam, S. & Scheres, S. H. W. High-throughput cryo-EM structure determination of amyloids. *Faraday Discuss.* **240**, 243–260 (2022).
62. Scheres, S. H. W. Amyloid structure determination in RELION-3.1. *Acta Crystallogr. D Struct. Biol.* **76**, 94–101 (2020).
63. Kimanius, D. et al. Data-driven regularization lowers the size barrier of cryo-EM structure determination. *Nat. Methods* **21**, 1216–1221 (2024).
64. Zivanov, J. et al. New tools for automated high-resolution cryo-EM structure determination in RELION-3. *eLife* **7**, e42166 (2018).
65. Pettersen, E. F. et al. UCSF Chimera—a visualization system for exploratory research and analysis. *J. Comput. Chem.* **25**, 1605–1612 (2004).
66. Emsley, P., Lohkamp, B., Scott, W. G. & Cowtan, K. Features and development of Coot. *Acta Crystallogr. D Biol. Crystallogr.* **66**, 486–501 (2010).
67. Adams, P. D. et al. PHENIX: a comprehensive Python-based system for macromolecular structure solution. *Acta Crystallogr. D Biol. Crystallogr.* **66**, 213–221 (2010).

Acknowledgements
We thank the participants and their families for donating brain tissues. We thank X. Qian for pathological evaluation, X. Wang, W. Ju, Y. Fu and H. Xiao for brain slide preparation and staining and N. Wang, D. Zhang and Z. Chen for obtaining tissue samples. We thank staff members in the National Human Brain Bank for Development and Function, Chinese Academy of Medical Science and Peking Union Medical College for brain sample preparation. We acknowledge the Cryo-EM center at the Interdisciplinary Research Center on Biology and Chemistry, Shanghai Institute of Organic Chemistry for help with data collection. We are grateful to M. Fändrich and L. Radamaker (Ulm University) for their help with the code to map the origin of the fibril segments in the cryo-EM micrographs. This work was supported by the National Natural Science Foundation of China (92353302 to D.L.; 82188101 and 22425704 to C.L.; 32170683 to D.L.), the Shanghai Basic Research Pioneer Project (to L.T. and C.L.), the Shanghai Pilot Program for Basic Research, Chinese Academy of Sciences, Shanghai Branch (CYJ-SHFY-2022-005 to C.L.), the Chinese Academy of Sciences Project for Young Scientists in Basic Research (YSBR-095 to C.L.), the Strategic Priority Research Program of the Chinese Academy of Sciences (XDB1060000 to C.L.), the Chinese Academy of Medical Science Innovation Fund for Medical Sciences (2021-I2M-1-025 to W.Q.) and the STI2030-Major Project (2021ZD0201100, task 1 2021ZD0201101 to W.Q.; 2021ZD0201100, task 1 2021ZD0201101 to C.M. and W.Q.). Dr. Cong Liu is a SANS Exploration Scholar.

Author contributions
Q.Z., C.L. and D.L. designed the project. W.Q., C.M., W.L., F.G. and Y.S. supplied human brain tissue. Q.Z. performed the IHC staining. S.L. and Y.Y. assisted with the staining process. Q.Z. and Y.T. prepared the cryo-EM samples and performed the cryo-EM data collection and processing. K.L., Y.Y., B.C. and T.C. helped with the cryo-EM data processing. W.X., Q.Z., Y.T. and C.W. performed the MS sample preparation, data acquisition and data processing. All authors were involved in analyzing the data and contributed to paper discussion and editing. Q.Z., Y.T., C.L. and D.L. wrote the paper.

Competing interests
The authors declare no competing interests.

Additional information
Extended data is available for this paper at https://doi.org/10.1038/s41589-025-01921-4.

Supplementary information The online version contains supplementary material available at https://doi.org/10.1038/s41589-025-01921-4.

Correspondence and requests for materials should be addressed to Wenying Qiu, Cong Liu or Dan Li.

Peer review information *Nature Chemical Biology* thanks Stefano Ricagno and the other, anonymous reviewer(s) for their contribution to the peer review of this work.

https://doi.org/10.1038/s41589-025-01921-4

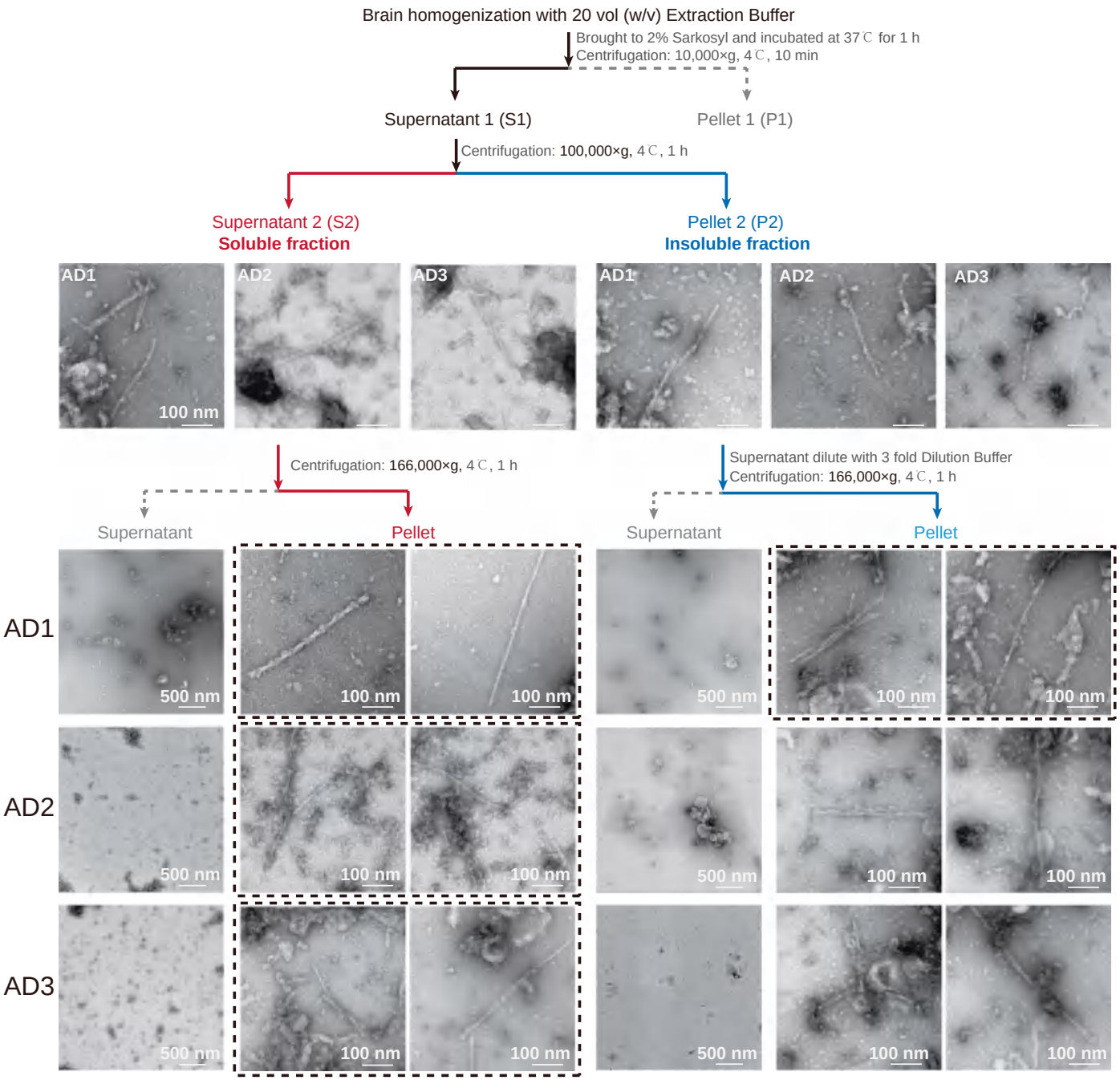

Extended Data Fig. 1 | Sarkosyl-based extraction of amyloid fibrils from the brains of three AD patients. Workflow of the extraction procedure and NS-TEM images of samples are shown. The solid arrows depict the steps with fibrils obtained: blue arrows highlight the purification steps for the sarkosyl-insoluble fraction (P2); red arrows highlight the purification steps for the sarkosyl-soluble fraction (S2). The grey dash arrows depict the steps with no fibril observed. Samples framed with dotted lines were used for further cryo- EM reconstruction.

https://doi.org/10.1038/s41589-025-01921-4

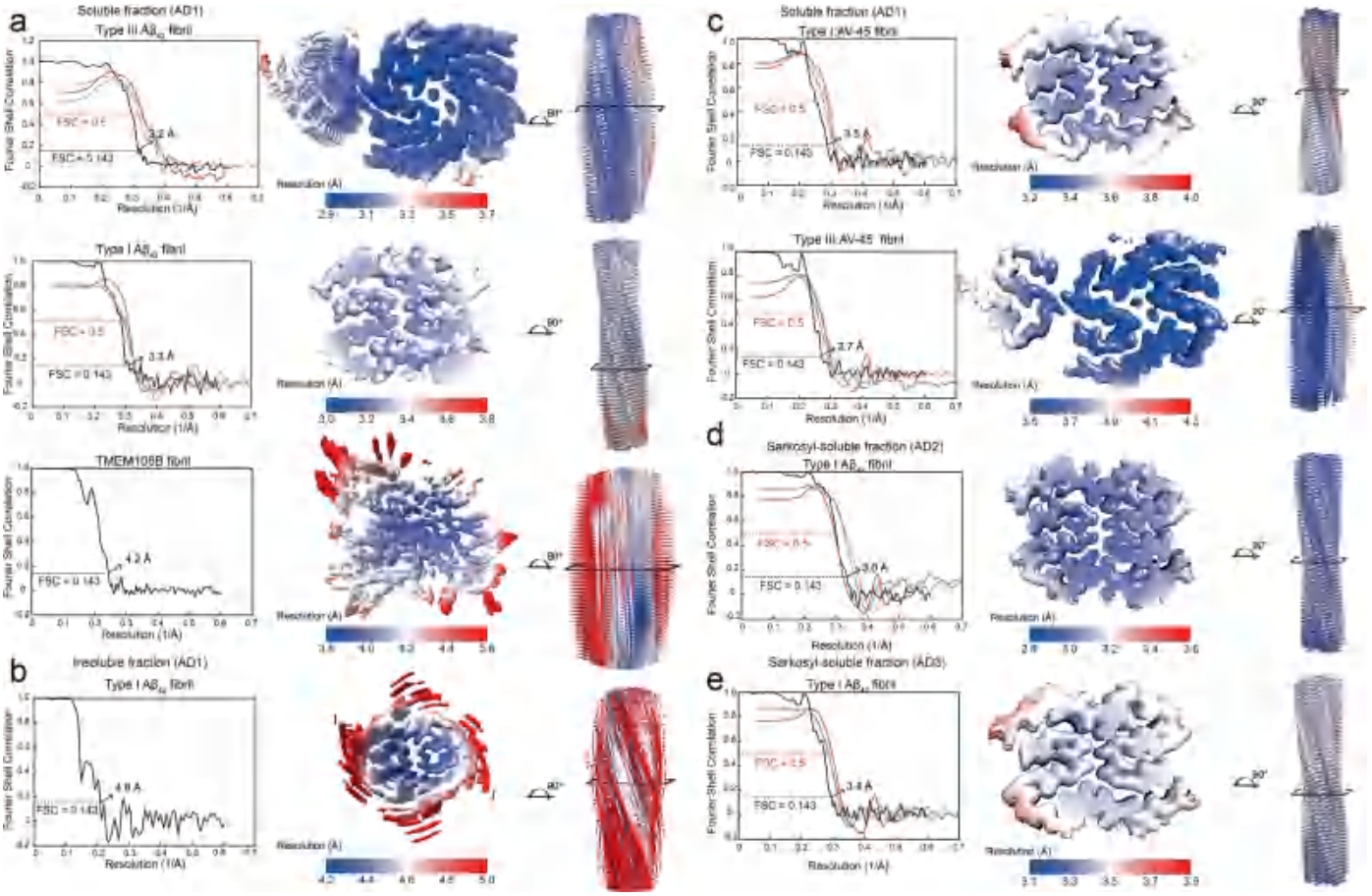

Extended Data Fig. 2 | Evaluation of the resolution of cryo-EM maps and refined models. Fourier shell correlation (FSC) curves for cryo-EM maps and corresponding structures of fibrils in (**a**) soluble, (**b**) insoluble fraction of AD1; (**c**) AV45 bound Aβ Type I and Type III fibrils in AD1; Type I in soluble fraction from (**d**) AD2 and (**e**) AD3 patients. The overall resolution was estimated based on gold-standard 0.143 Fourier shell correlation (FSC) of two independently refined cryo-EM half maps, which are shown in black; for the final refined atomic model against final cryo-EM map shown in red; for the refined atomic model against the two half maps depicted in orange and blue dotted lines, respectively. The local resolution plots of the recombinant 3D density maps are estimated by the 'Local resolution' program in RELION 4.0.

https://doi.org/10.1038/s41589-025-01921-4

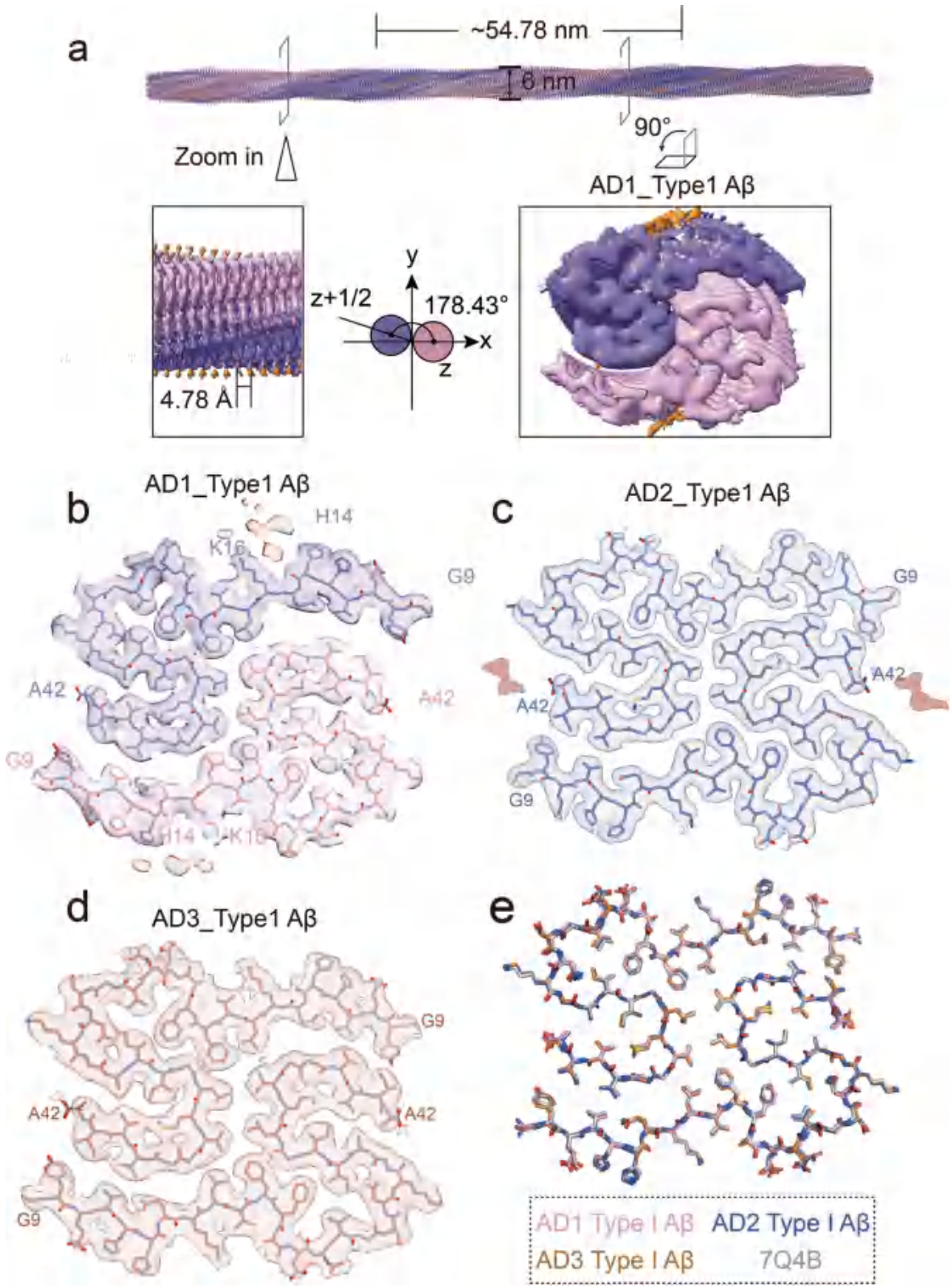

Extended Data Fig. 3 | Cryo-EM structures of the Type I Aβ42 fibrils in the soluble fraction of the AD brains. a. Density map of the Type I Aβ42 fibril in the soluble fraction of the AD1 brain. The two protofilaments were colored in purple and pink, respectively. The map shows one crossover (360° helical turn) of the fibril. Zoomed-in side view and cross- section view are shown below. The fibrill width and helical parameters of the fibril are indicated. Extra densities are colored in orange. **b-d.** Structural models of Type I Aβ42 fibrils obtained from AD1 (**b**), AD2 (**c**) and AD3 (**d**) are fitted in their density maps. The density maps are restricted to areas within 2 Å radius of the structural models. Extra densities are colored in orange. **e.** Structure comparison of the Type I Aβ42 fibrils obtained from the soluble fraction of the brains of AD1-3 cases (this work) and that obtained from the insoluble fraction of AD brains (PDB ID: 7Q4B). r.m.s.d. for AD1 (pink) versus AD2 (blue): 0.191 over 63 Cα atoms; AD1 versus AD3 (orange): 0.145 over 61 Cα atoms; AD1 versus 7Q4B (gray): 0.398 over 67 Cα atoms (global alignments).

https://doi.org/10.1038/s41589-025-01921-4

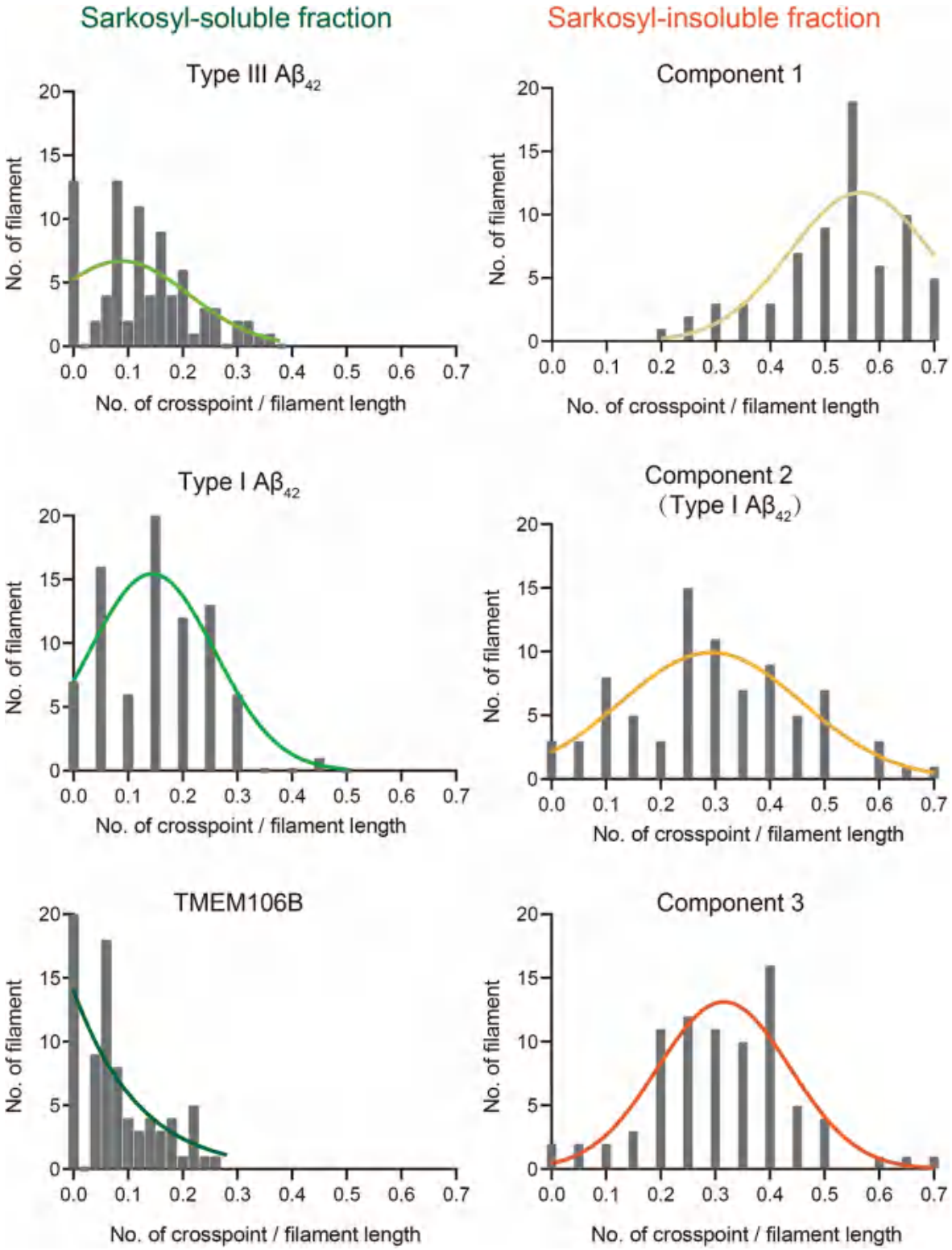

Extended Data Fig. 4 | Histograms of the distribution of crossover points per unit length for each type of fibrils. For each fibril type, n = 80 fibrils. The fitted Gaussians lines are colored in consistent with Fig. 3.

https://doi.org/10.1038/s41589-025-01921-4

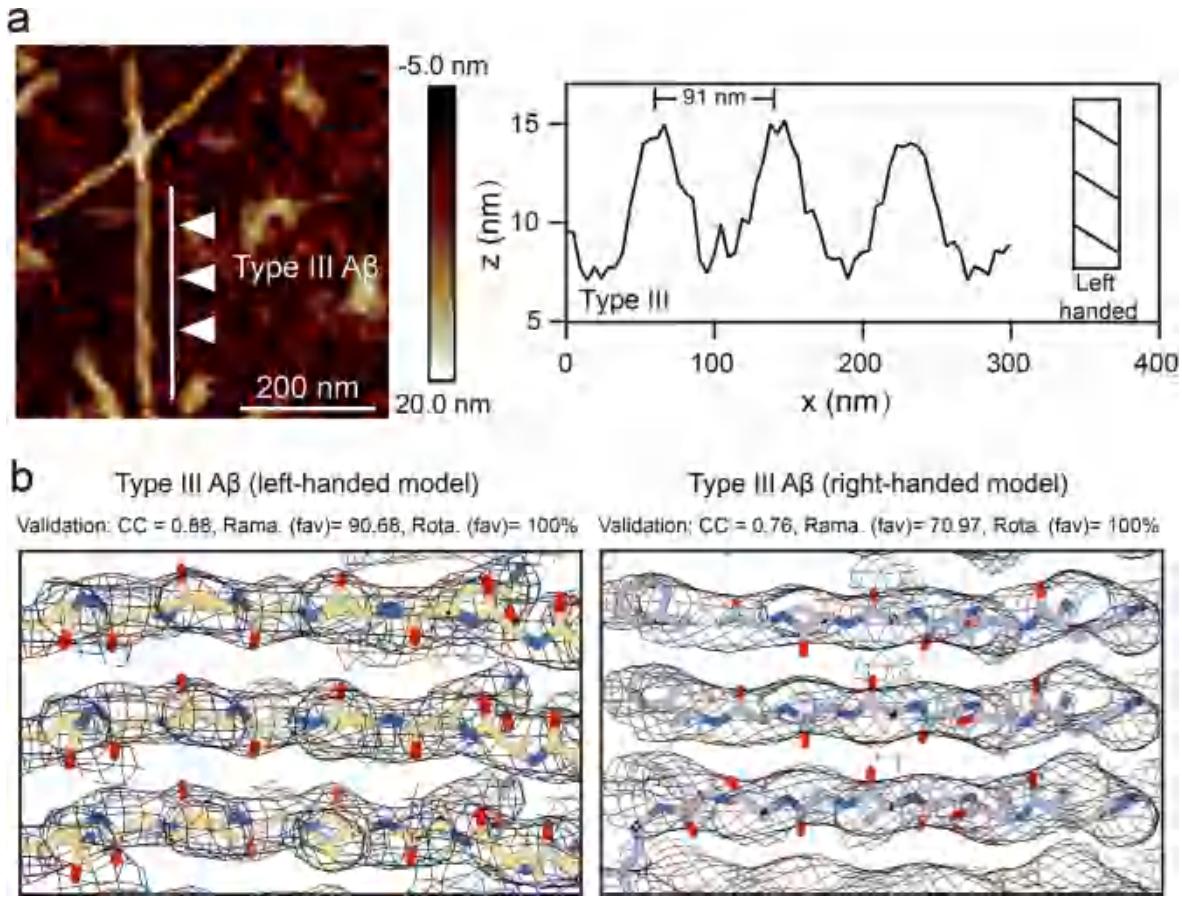

Extended Data Fig. 5 | Handedness characterization for Type III Aβ42 fibril. **a**. Atomic force microscopic (AFM) image (left) of the Type III Aβ42 fibril. Analysis of the periodic spacing along the fibril, indicated with a white line and arrowheads on the image, is shown on the right. Graphic illustration of fibril chirality is shown. **b**. Cryo-EM density of central β-strand segments of the Type III Aβ42 fibril with structural model fitted in. The density map was determined with left-handed (left) and right-handed (right) helical parameters, respectively. Correspondingly, a refined left-handed or right-handed structural model was fitted in. The backbone carbonyls fit the density better in the left-handed model as validated by the post real-space refinement statistics indicated on the top. CC, correlation coefficient between the masked map and the model; Rama., favored Ramachandran orientations; Rota., favored rotamer orientations.

https://doi.org/10.1038/s41589-025-01921-4

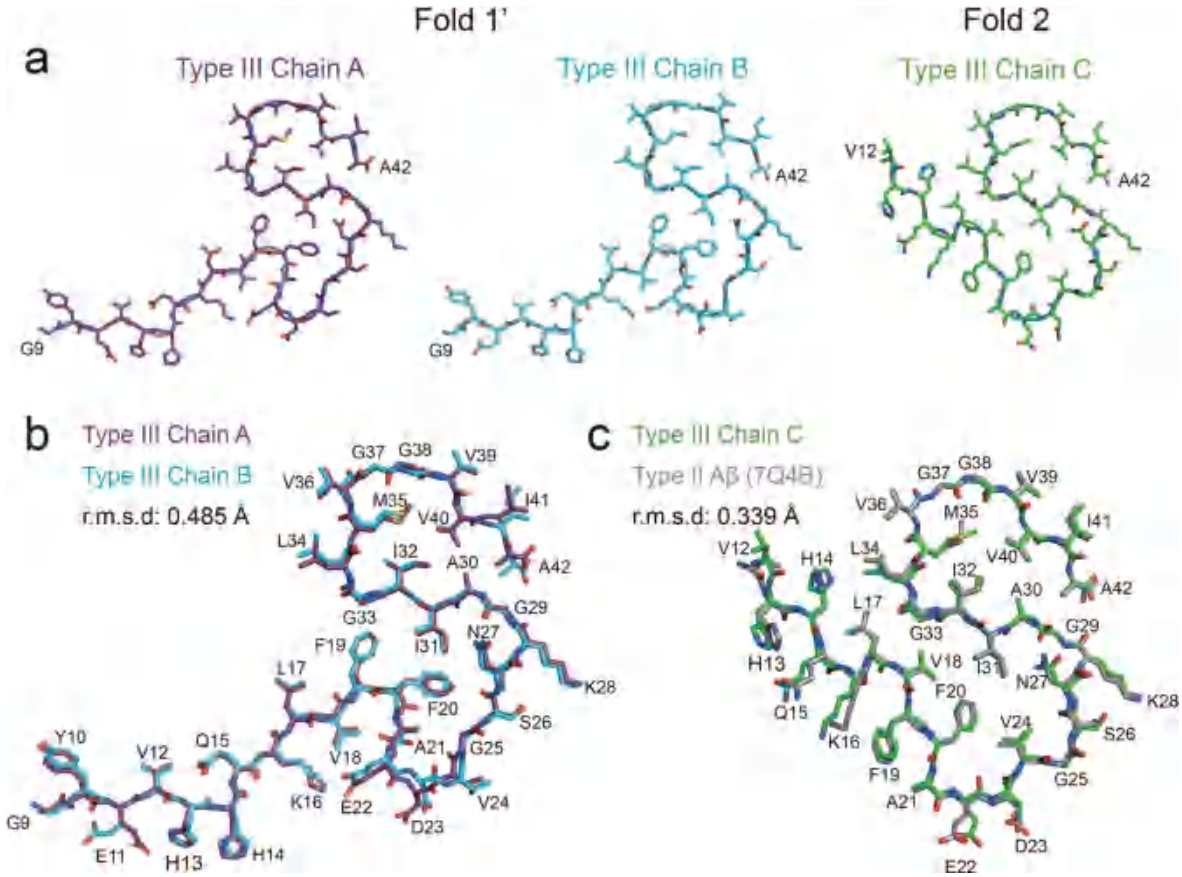

Extended Data Fig. 6 | Type III Aβ42 fibril forms two distinct folds. a The models of three protofilaments Type III Aβ42 fibril can be divided into two folds, fold 1' (composing Chain A and Chain B) and fold 2 (Chain C). Three protofilaments are aligned separately in the same 'S-shape' orientation, shown in sticks and cartoon loop, and then colored in purple (Chain A), cyan (Chain B) and green (Chain C), respectively. **b** Structure comparison of two protofilaments, Chain A (purple) and Chain B (cyan) structures in Type III Aβ42 fibril. The structural models are shown in sticks, with all the residues labeled. Global alignments (9-42) indicated the r.m.s.d of Type III Chain A versus Chain B is 0.485 Å over 32 Cα atoms. **c** Type III chain C and Type II Aβ42 protofilament previous reported (PDB: 7Q4B) are overlaid and colored in green and grey, respectively. The r.m.s.d between two protofilaments is 0.339 over 30 Cα atoms (global alignments).

https://doi.org/10.1038/s41589-025-01921-4

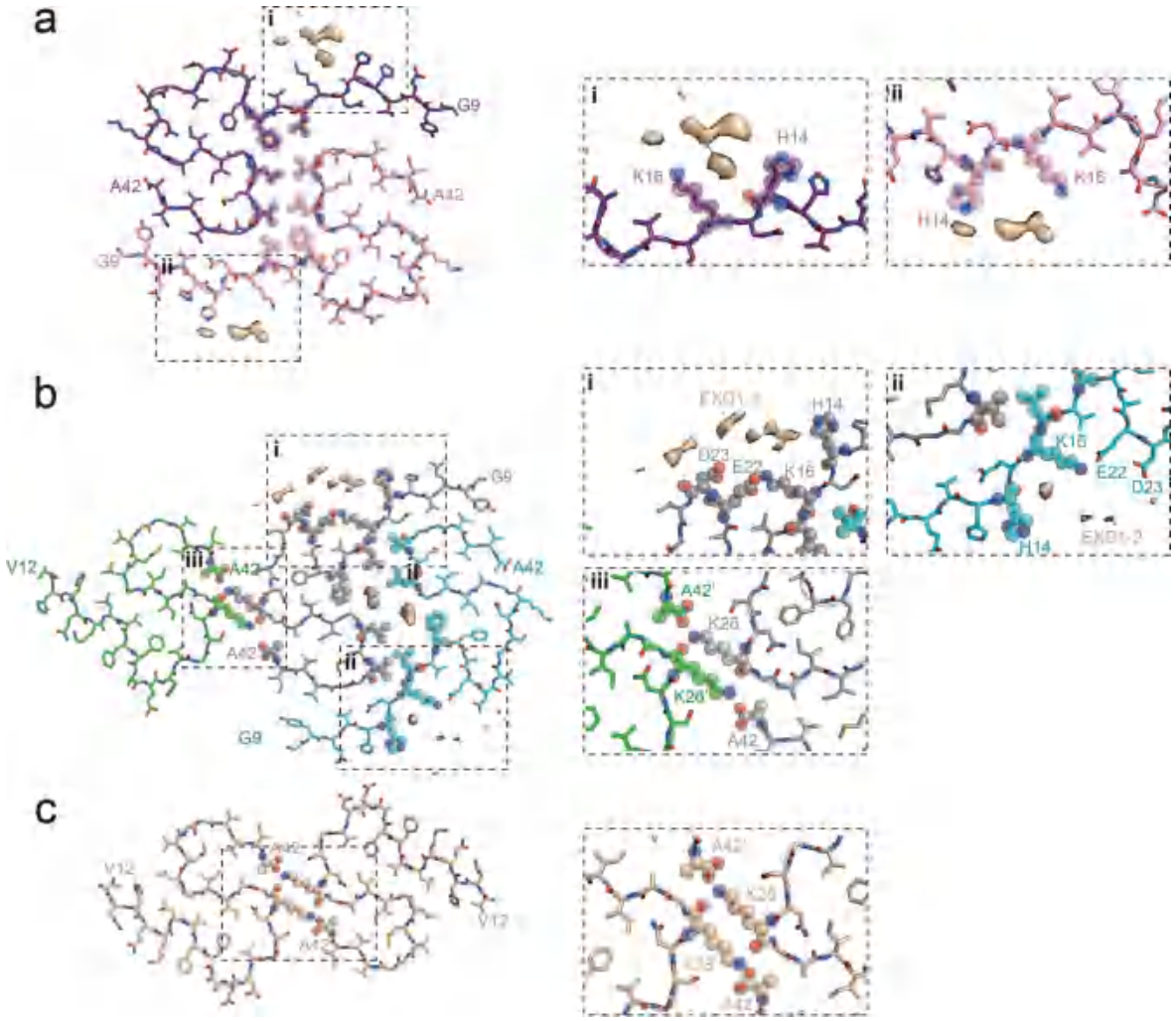

Extended Data Fig. 7 | Comparison of extra densities in the Aβ42 fibrils. Structures of the Type I (**a**) and the Type III (**b**) fibrils extracted from the soluble fraction of AD1, and the Type II fibril (PDB:7Q4B) (**c**) are shown. One layer of Aβ42 structure in each fibril is shown. Residues composing the protofilamental interface are shown in spheres in the left panels. Extra densities are shown in orange and zoomed in on the right, where residues surround the extra densities are labeled and highlighted in spheres.

https://doi.org/10.1038/s41589-025-01921-4

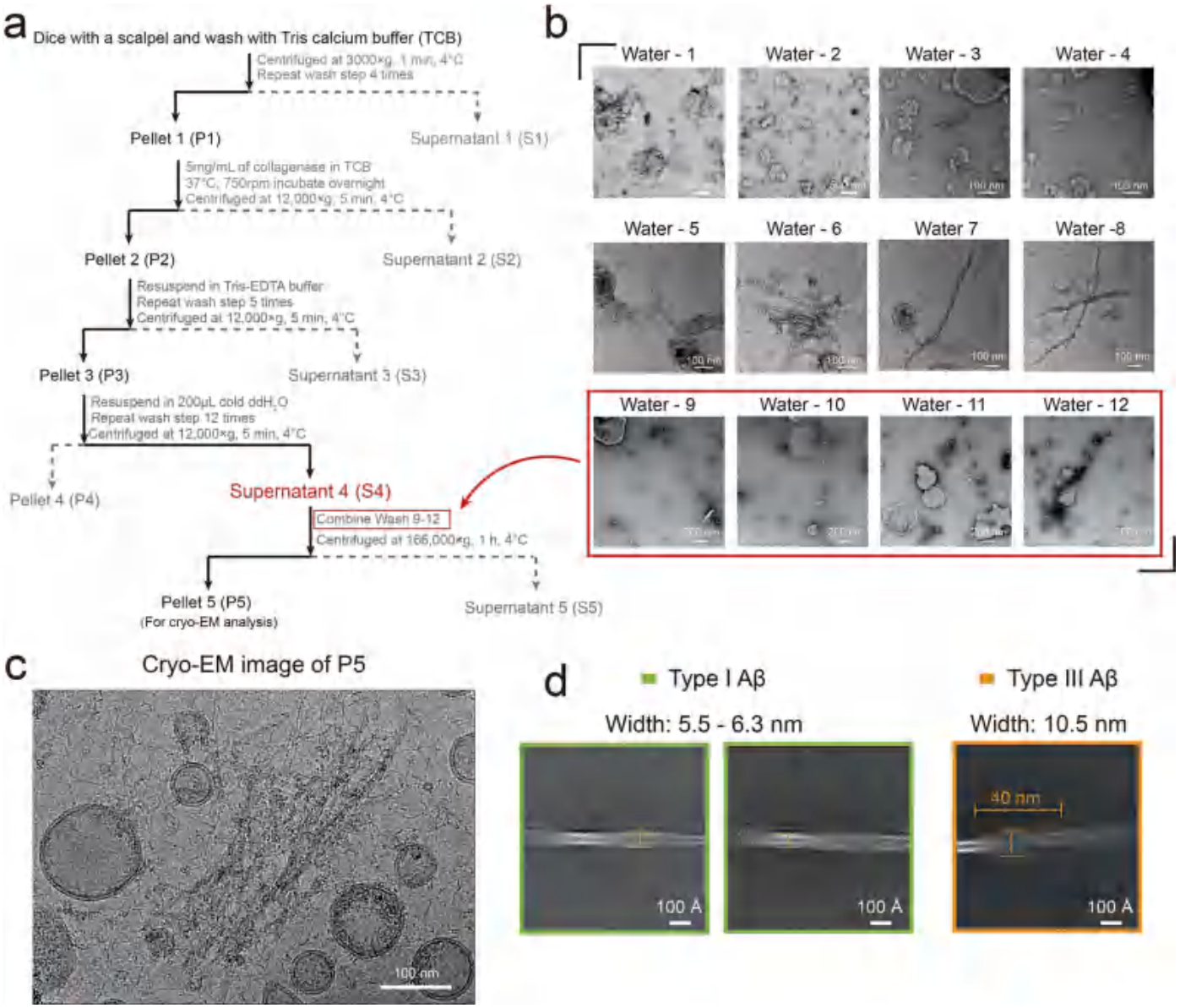

Extended Data Fig. 8 | Cryo-EM analysis for ex vivo fibrils extracted from AD1 by using water-based extraction method. a Workflow of the water-based fibril extraction procedure. Solid arrows depict the steps used in the next step. P5 was used for cryo-EM analysis. **b** NS-TEM images of the supernatants of the 12-time repeat wash highlighted in (**a**). Samples 9–12 framed with a red frame were combined as S4. **c** Representative cryo-EM micrograph of P5 from one of 16,305 movies. **d** The 3 most populated 2D class averages of fibrils in P5. Fibril polymorph was determined based on the crossover distance (pitch), fibril width and morphology. Type I fibrils are labeled in green; Type III fibrils are labeled in orange. Constructed using 2× binned particles of the full set of segments after the removal of picking artifacts. The box size is ~87 nm.

https://doi.org/10.1038/s41589-025-01921-4

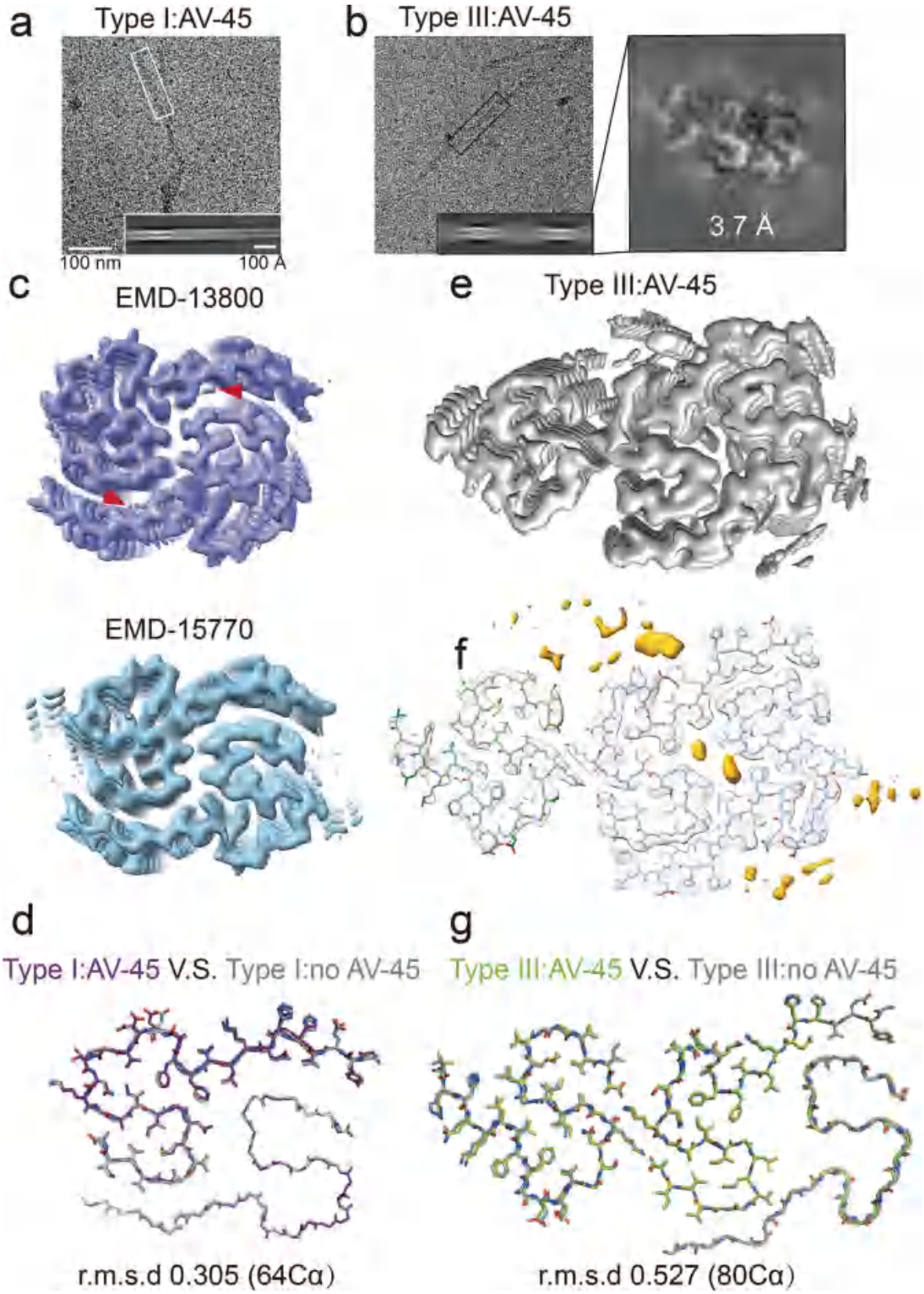

Extended Data Fig. 9 | See next page for caption.

https://doi.org/10.1038/s41589-025-01921-4

Extended Data Fig. 9 | Structural characterization and comparison of ex vivo Aβ42 fibrils after incubating with AV-45. a., b. Representative cryo-EM micrographs of AD1 soluble Type I (**a**) and Type III (**b**) fibrils incubated with AV-45. Insets: 2D class averages. **c** Cross-section of density maps from previously reported ex vivo Aβ42 fibrils extracted from the brains of sporadic AD patients by sarkosyl-based extraction method (top, EMD-ID: EMD-13800) and water-based soaking method (bottom, EMD- ID: EMD-15770). Potential solvent densities in the AV-45 binding channel are indicated in red arrow heads. **d** Structural comparison between the soluble Type I fibrils of AD1 with and without the addition of AV-45. One half of structural model is shown in sticks, and the other half is shown by main chains. R.m.s.d. between these two structures is 0.305 over 64 Cα atoms (global alignments).**e., f.** Cross-section view of the Type III:AV-45 complex density map (**e**) and the structural model fitted in the density map within 2-Å radius of the model (**f**). Extra densities are colored in orange. **g.** Structural comparison between the Type III fibrils of AD1 with and without the addition of AV-45. The r.m.s.d. between the two structures is 0.527 over 80 Cα atoms (global alignments).

https://doi.org/10.1038/s41589-025-01921-4

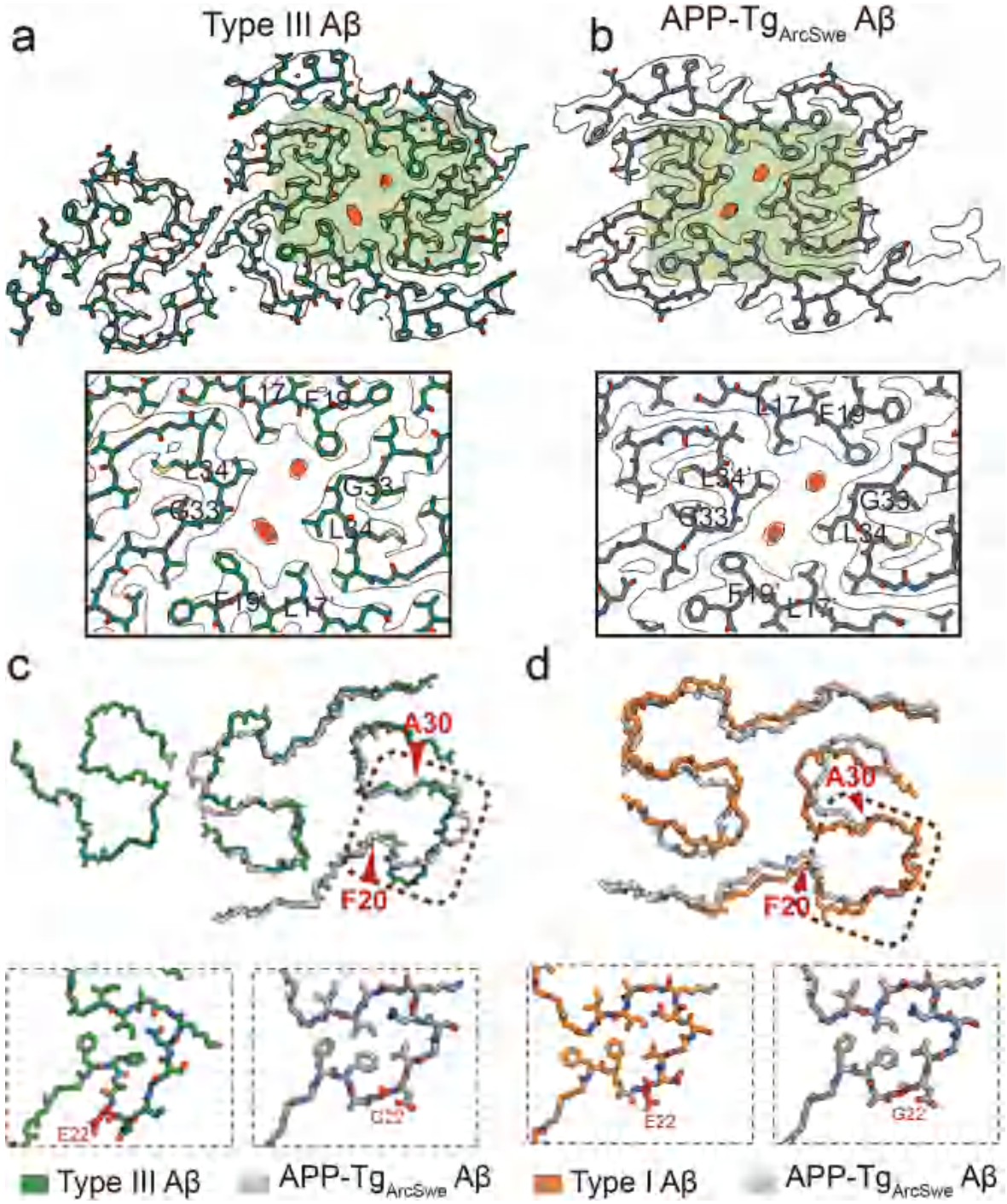

Extended Data Fig. 10 | Structural comparison of tg-APPArcSwe fibril and AD Type I and III Aβ42 fibrils. a., b. Structural models of Type III Aβ42 (a) and tg-APPArcSwe (b) fibrils fitted in their density maps. The density map is restricted to areas within 2-Å radius of the structural model. The protofilamental interfaces enclosing extra densities were shaded in green and zoomed in. Extra densities of cofactors are colored in orange. **c.** Structural comparison of the Type III Aβ42 fibrils and tg-APPArcSwe Aβ fibril (PDB ID: 8OL7). R.m.s.d.= 1.17 Å over 23 Cα atoms. Segment F20-A30 is framed with dotted box and zoomed in below with E22G mutation in mouse Aβ labeled. **d** Structural comparison of the Type I Aβ42 fibrils and tg-APPArcSwe Aβ fibril. R.m.s.d.= 0.145 over 61 Cα atoms.

nature portfolio

Corresponding author(s): Dan Li, Cong Liu, Wenying Qiu

Last updated by author(s): July 13, 2024

Reporting Summary

Nature Portfolio wishes to improve the reproducibility of the work that we publish. This form provides structure for consistency and transparency in reporting. For further information on Nature Portfolio policies, see our Editorial Policies and the Editorial Policy Checklist.

Statistics

For all statistical analyses, confirm that the following items are present in the figure legend, table legend, main text, or Methods section.

n/a	Confirmed
☐	☒ The exact sample size (*n*) for each experimental group/condition, given as a discrete number and unit of measurement
☐	☒ A statement on whether measurements were taken from distinct samples or whether the same sample was measured repeatedly
☒	☐ The statistical test(s) used AND whether they are one- or two-sided *Only common tests should be described solely by name; describe more complex techniques in the Methods section.*
☒	☐ A description of all covariates tested
☒	☐ A description of any assumptions or corrections, such as tests of normality and adjustment for multiple comparisons
☐	☒ A full description of the statistical parameters including central tendency (e.g. means) or other basic estimates (e.g. regression coefficient) AND variation (e.g. standard deviation) or associated estimates of uncertainty (e.g. confidence intervals)
☒	☐ For null hypothesis testing, the test statistic (e.g. *F*, *t*, *r*) with confidence intervals, effect sizes, degrees of freedom and *P* value noted *Give P values as exact values whenever suitable.*
☒	☐ For Bayesian analysis, information on the choice of priors and Markov chain Monte Carlo settings
☒	☐ For hierarchical and complex designs, identification of the appropriate level for tests and full reporting of outcomes
☒	☐ Estimates of effect sizes (e.g. Cohen's *d*, Pearson's *r*), indicating how they were calculated

Our web collection on statistics for biologists contains articles on many of the points above.

Software and code

Policy information about availability of computer code

Data collection	EPU 2.11.1.
Data analysis	Relion 3.1, Relion5.0, MotionCorr2 1.2.1, CTFFIND-4.1.8, WinCoot 0.8.9.2, PHENIX 1.13, SMILES, PyMOL v1.7.4.5., UCSF Chimera 1.13.1, ChimeraX 1.5, GraphPad Prism 8, Adobe Illustrator 2019, pFind 3.2.0, Unimod (Accession #:617), Maxquant (2.2.0.0), NanoScope Analysis software (version 1.5).

For manuscripts utilizing custom algorithms or software that are central to the research but not yet described in published literature, software must be made available to editors and reviewers. We strongly encourage code deposition in a community repository (e.g. GitHub). See the Nature Portfolio guidelines for submitting code & software for further information.

Data

Policy information about availability of data

All manuscripts must include a data availability statement. This statement should provide the following information, where applicable:

- Accession codes, unique identifiers, or web links for publicly available datasets
- A description of any restrictions on data availability
- For clinical datasets or third party data, please ensure that the statement adheres to our policy

The cryo-EM maps have been deposited in the Electron Microscopy Data Bank (EMDB) under accession numbers EMD-37170 for AD1 Type I Aβ42 fibril of soluble fraction, EMD-37197 for AD1 Type III Aβ42 fibril of soluble fraction, EMD-37195 for Type I:AV-45 complex, EMD-37200 for Type III:AV-45 complex, EMD-37198 for

AD2 Type I Aβ42 fibril of soluble fraction and EMD-37199 for AD3 Type I Aβ42 fibril of soluble fraction. The corresponding refined atomic models of the AD1 Type I, AD3 Type III Aβ42, Type I:AV-45, Type III:AV-45, AD2 Type I and AD3 Type I fibril have been deposited in the Protein Data Bank (PDB) following accession numbers 8KEW, 8KF3, 8KF1, 8KF6, 8KF4 and 8KF5, respectively. The density maps used are available in EMDB databased under accession number EMD-33055 (Type 3 TMEM106B fibril). The structural models used in this study are available in the PDB database under accession codes 7Q4B (Type I Aβ42 fibril) and 7Q4M (Type II Aβ42 fibril). All raw data, including western blots are available within the paper and Supplementary Information files. The search was performed against the reviewed UniProt Human protein database.

Research involving human participants, their data, or biological material

Policy information about studies with human participants or human data. See also policy information about sex, gender (identity/presentation), and sexual orientation and race, ethnicity and racism.

Reporting on sex and gender	See method section and Table 1, Gender: 2x male, 1x femal.
Reporting on race, ethnicity, or other socially relevant groupings	No reporting on race, ethnicity, or other socially relevant grouping was performed.
Population characteristics	See Table 1 and method section, "Post-mortem human brain samples". Diagnoses: 3x AD. Age at Death: 83, 84, 89.
Recruitment	Sample were selected based on neuropathological examination and brain tissue availability.
Ethics oversight	The subjects of this study were three clinically diagnosed Alzheimer's disease cases. Ethical approval was obtained from the Institutional Review Board of the Institute of Basic Medical Sciences, Chinese Academy of Medical Sciences (Approval Numbers: 009-2014, 031–2017, 2022125). All AD brain samples were provided by the National Human Brain Bank for Development and Function, Chinese Academy of Medical Science and Peking Union Medical College, Beijing, China.

Note that full information on the approval of the study protocol must also be provided in the manuscript.

Field-specific reporting

Please select the one below that is the best fit for your research. If you are not sure, read the appropriate sections before making your selection.

☒ Life sciences ☐ Behavioural & social sciences ☐ Ecological, evolutionary & environmental sciences

For a reference copy of the document with all sections, see nature.com/documents/nr-reporting-summary-flat.pdf

Life sciences study design

All studies must disclose on these points even when the disclosure is negative.

Sample size	This is mainly a structure and biochemistry study. Three brain samples: frontal cortex are chosed based on availability of tissues (maximum available sample size). The amounts of cryo-EM micrographs collected were sufficient to generate high-resolution densities. Details of cryo-EM datasets are given in Methods and Supplementary Table 1.
Data exclusions	None.
Replication	All attempts at replication were successful. Experiments results were robust and reproducible. Western blot and immunogold labeling experiments were performed at least three times independently. Cryo-EM structure determination and mass spectrometric analysis for the same patient sample was not replicated due to tissue limitations and intensive nature of experiments.
Randomization	This study was not related to randomization. No animal or human studies were involved. The sample size (available tissues) was not large enough to require random sampling. Thus, it is well accepted and an established notion that randomization is not relevant to the structural studies.
Blinding	Blinding was not performed during experiments and outcome assessment. The perceived risk of detection/performance bias was deemed negligible.

Reporting for specific materials, systems and methods

We require information from authors about some types of materials, experimental systems and methods used in many studies. Here, indicate whether each material, system or method listed is relevant to your study. If you are not sure if a list item applies to your research, read the appropriate section before selecting a response.

Materials & experimental systems

n/a	Involved in the study
☐	☒ Antibodies
☒	☐ Eukaryotic cell lines
☒	☐ Palaeontology and archaeology
☒	☐ Animals and other organisms
☒	☐ Clinical data
☒	☐ Dual use research of concern
☒	☐ Plants

Methods

n/a	Involved in the study
☒	☐ ChIP-seq
☒	☐ Flow cytometry
☒	☐ MRI-based neuroimaging

Antibodies

Antibodies used

Primary antibodies used were presented in the Methods section with validation referenced. They are:
(1) anti-TMEM106B, Novus biologicals, catalog No. NBP1-91311, Lot No. QC77795-221103 (1:250 dilution for immunohistochemistry);
(2) anti-β-Amyloid, x-42 Antibody, Biolegend, catalog No. 812101, Clone: Lot No. B370870 (1:250 dilution for immunohistochemistry; 1:2000 for Western blot);
(3) anti-β-Amyloid, 1-40 Antibody, Biolegend, catalog No. 867801, Clone: 11A50-B10, Lot No. B377529 (1:1000 dilution for immunohistochemistry);
(4) anti-β-Amyloid, 1-16 Antibody, Biolegend, catalog No. 867801, Clone: 6E10, Lot No.B378931 (1:2000 dilution for Western blot);
(5) Phospho-Tau (Ser202, Thr205) Monoclonal Antibody (AT8), Invitrogen, catalog No. MN1020, Clone: AT8, Lot No.ZB4164363 (1:1000 dilution for immunohistochemistry);
(6) anti-α-Synuclein Antibody, Biolegend, catalog No. MMS-5085, Clone: Syn303, Lot No.B399035 (1:250 dilution for immunohistochemistry).
(7) Goat anti-Mouse IgG (H+L) Cross-Adsorbed Secondary Antibody, Alexa Fluor™ 594, Invitrogen, catalog No. A-21207, Lot No. 2747441 (1:1000 dilution for immunoflourescence).
(8) Goat Anti-Mouse IgG Antibody (H+L), Biotinylated, Vector laboratories, catalog No. BA-9200, Lot No. Z J1020 (1:1000 dilution for immunohistochemistry)
(9) Goat Anti-Rabbit IgG Antibody (H+L), Biotinylated, Vector laboratories, catalog No. BA-1000, Lot No. Z F043 (1:1000 dilution for immunohistochemistry)

Validation

The antibody validation is presented in the manufacturer's datasheet (Novus, Biolegend, Invitrogen).
(1) Species reactivity: mouse; host/isotype: rabbit/IgG; validation: western blot by Novus Biologicals; application: western blot.
(2)Species reactivity: Human; host/isotype: rabbit/IgG; validation: IHC staining by Biolegend; application: IHC-P, western blot.
(3)Species reactivity: Human; host/isotype: mouse/IgG1, κ; validation: IHC staining by Biolegend; application: IHC-P, DOT Blot, ELISA
(4)Species reactivity: Human; host/isotype: mouse/IgG1, κ; validation: western blot, Direct ELISA and IHC-P by Biolegend; application: WB, Direct ELISA, IHC-P, IHC-F, EM.
(5)Species reactivity: Human; host/isotype: mouse/IgG1, κ; validation: IHC staining by Invitrogen; application: western blot, IHC-P/F, IHC-Free, ICC/IF, Flow, ELISA, IP, PLA, DB, UA,IDF and Misc.
(6) Species reactivity: Human; host/isotype: mouse/IgG1, κ; validation: IHC staining by Biolegend; application: IHC-P.

Plants

Seed stocks

None.

Novel plant genotypes

None.

Authentication

None.